


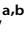

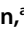






# Metabolic Remodeling during Nitrogen Fixation in *Zymomonas mobilis*

 Julia I. Martien,<sup>a,b</sup>  Edna A. Trujillo,<sup>c,d</sup>  Tyler B. Jacobson,<sup>a,b</sup>  Mehmet Tatli,<sup>a,b</sup>  Alexander S. Hebert,<sup>a,c</sup>  David M. Stevenson,<sup>a,b</sup>  
 Joshua J. Coon,<sup>a,c,d,e,f</sup>  Daniel Amador-Noguez<sup>a,b</sup>

<sup>a</sup>DOE Great Lakes Bioenergy Research Center, University of Wisconsin–Madison, Madison, Wisconsin, USA

<sup>b</sup>Department of Bacteriology, University of Wisconsin–Madison, Madison, Wisconsin, USA

<sup>c</sup>Department of Chemistry, University of Wisconsin–Madison, Madison, Wisconsin, USA

<sup>d</sup>National Center for Quantitative Biology of Complex Systems, University of Wisconsin–Madison, Madison, Wisconsin, USA

<sup>e</sup>Department of Biomolecular Chemistry, University of Wisconsin–Madison, Madison, Wisconsin, USA

<sup>f</sup>Morgridge Institute for Research, Madison, Wisconsin, USA

**ABSTRACT** *Zymomonas mobilis* is an ethanologenic bacterium currently being developed for production of advanced biofuels. Recent studies have shown that *Z. mobilis* can fix dinitrogen gas (N<sub>2</sub>) as a sole nitrogen source. During N<sub>2</sub> fixation, *Z. mobilis* exhibits increased biomass-specific rates of ethanol production. In order to better understand the physiology of *Z. mobilis* during N<sub>2</sub> fixation and during changes in ammonium (NH<sub>4</sub><sup>+</sup>) availability, we performed liquid chromatography-mass spectrometry (LC-MS)-based targeted metabolomics and shotgun proteomics under three regimes of nitrogen availability: continuous N<sub>2</sub> fixation, gradual NH<sub>4</sub><sup>+</sup> depletion, and acute NH<sub>4</sub><sup>+</sup> addition to N<sub>2</sub>-fixing cells. We report dynamic changes in abundance of proteins and metabolites related to nitrogen fixation, motility, ammonium assimilation, amino acid biosynthesis, nucleotide biosynthesis, isoprenoid biosynthesis, and Entner-Doudoroff (ED) glycolysis, providing insight into the regulatory mechanisms that control these processes in *Z. mobilis*. Our analysis identified potential physiological mechanisms that may contribute to increased specific ethanol production during N<sub>2</sub> fixation, including decreased activity of biosynthetic pathways, increased protein abundance of alcohol dehydrogenase (ADHI), and increased thermodynamic favorability of the ED pathway. Of particular relevance to advanced biofuel production, we found that intermediates in the methylerythritol phosphate (MEP) pathway for isoprenoid biosynthesis were depleted during N<sub>2</sub> fixation, coinciding with decreased protein abundance of deoxyxylulose 5-phosphate synthase (DXS), the first enzyme in the pathway. This implies that DXS protein abundance serves as a native control point in regulating MEP pathway activity in *Z. mobilis*. The results of this study will inform metabolic engineering to further develop *Z. mobilis* as a platform organism for biofuel production.

**IMPORTANCE** Biofuels and bioproducts have the potential to serve as environmentally sustainable replacements for petroleum-derived fuels and commodity molecules. Advanced fuels such as higher alcohols and isoprenoids are more suitable gasoline replacements than bioethanol. Developing microbial systems to generate advanced biofuels requires metabolic engineering to reroute carbon away from ethanol and other native products and toward desired pathways, such as the MEP pathway for isoprenoid biosynthesis. However, rational engineering of microbial metabolism relies on understanding metabolic control points, in terms of both enzyme activity and thermodynamic favorability. In *Z. mobilis*, the factors that control glycolytic rates, ethanol production, and isoprenoid production are still not fully understood. In this study, we performed metabolomic, proteomic, and thermodynamic analysis of *Z. mobilis* during N<sub>2</sub> fixation. This analysis identified key changes in

**Citation** Martien JI, Trujillo EA, Jacobson TB, Tatli M, Hebert AS, Stevenson DM, Coon JJ, Amador-Noguez D. 2021. Metabolic remodeling during nitrogen fixation in *Zymomonas mobilis*. mSystems 6:e00987-21. <https://doi.org/10.1128/mSystems.00987-21>.

**Editor** Claudia Vickers, CSIRO

**Copyright** © 2021 Martien et al. This is an open-access article distributed under the terms of the [Creative Commons Attribution 4.0 International license](https://creativecommons.org/licenses/by/4.0/).

Address correspondence to Daniel Amador-Noguez, [amadornoguez@wisc.edu](mailto:amadornoguez@wisc.edu).

**Received** 28 July 2021

**Accepted** 6 October 2021

**Published** 16 November 2021

metabolite levels, enzyme abundance, and glycolytic thermodynamic favorability that occurred during changes in  $\text{NH}_4^+$  availability, helping to inform future efforts in metabolic engineering.

**KEYWORDS** MEP pathway, *Zymomonas mobilis*, biofuels, isoprenoids, metabolomics, nitrogen fixation, nitrogen metabolism, proteomics, systems biology, thermodynamics

**Z***ymomonas mobilis* has long been recognized as a promising platform organism for biofuel production (1–3). A combination of high glucose tolerance, rapid glucose consumption, and high ethanol yield (over 90% theoretical maximum) make *Z. mobilis* comparable or even superior to *Saccharomyces cerevisiae* in its native ability to produce bioethanol (4–6). Ongoing efforts in metabolic engineering aim to further increase the utility of *Z. mobilis* as a biofuel producer by expanding its substrate utilization, improving its stress tolerance, and diversifying its product profiles to include more valuable products such as higher alcohols and isoprenoids (7–16, 114, 115).

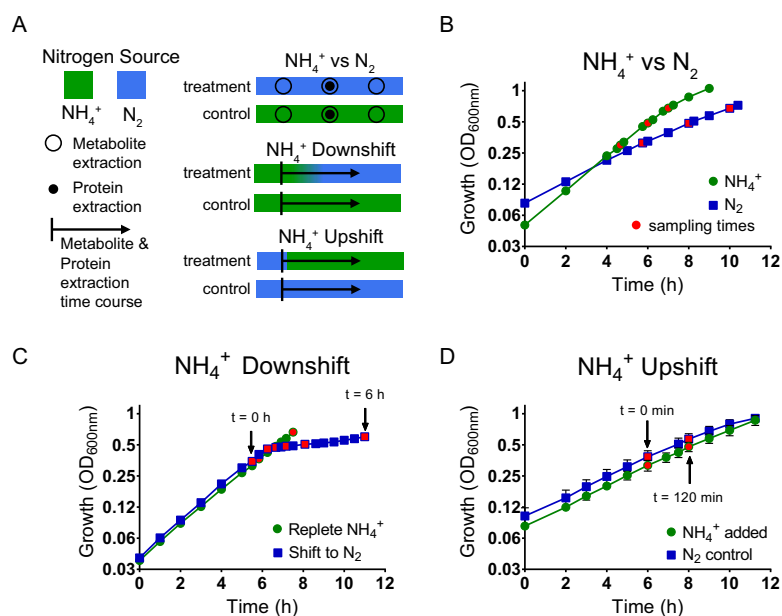
Recently, it was demonstrated that *Z. mobilis* is capable of fixing dinitrogen gas ( $\text{N}_2$ ) as a sole nitrogen source (17). The ability to utilize  $\text{N}_2$  gas rather than bioavailable nitrogen supplements offers a clear advantage for lignocellulosic biofuel production in terms of both economic viability and environmental sustainability (17, 18). However, little is known about the physiology of *Z. mobilis* during  $\text{N}_2$  fixation. Previous studies have shown that during  $\text{N}_2$  fixation, *Z. mobilis* exhibits a lower growth rate and lower growth yield but a higher biomass-specific ethanol production rate, higher specific glucose consumption rate, and equivalent or slightly higher ethanol yield (17, 19, 20). This is a striking observation considering the already highly catabolic metabolism employed by *Z. mobilis* during replete ammonium ( $\text{NH}_4^+$ ) availability (21). Increased glucose uptake and ethanol production imply major metabolic remodeling. However, the underlying physiological changes that occur during  $\text{N}_2$  fixation, including changes in protein expression and intracellular metabolite abundance, are currently unknown.  $\text{N}_2$  fixation therefore provides a unique system in which to examine native metabolic regulation in *Z. mobilis* and identify metabolic engineering strategies to maximize production of target molecules.

In this study, we measured relative protein abundance and relative abundance of intracellular metabolites using liquid chromatography coupled to mass spectrometry (LC-MS) (22, 23). LC-MS-based targeted metabolomics and shotgun proteomics were performed during continuous  $\text{N}_2$  fixation and during dynamic changes in  $\text{NH}_4^+$  availability. This analysis expands the current understanding of *Z. mobilis* physiology and provides new information regarding the native regulation of biofuel-producing pathways.

## RESULTS AND DISCUSSION

**Experimental design and nitrogen availability regimes.** We quantified relative metabolite and protein abundance under  $\text{N}_2$ -fixing conditions in comparison to  $\text{NH}_4^+$ -replete conditions and during transitions between these two growth conditions. *Z. mobilis* (ATCC 31821) was grown anaerobically using glucose as the sole carbon source (see Materials and Methods) (24). For conditions of replete  $\text{NH}_4^+$  availability, 15 mM  $\text{NH}_4^+$  was provided. For  $\text{N}_2$ -fixing conditions, no  $\text{NH}_4^+$  was added to the medium and the only available nitrogen source was  $\text{N}_2$  gas (>90%  $\text{N}_2$  in the anaerobic chamber).

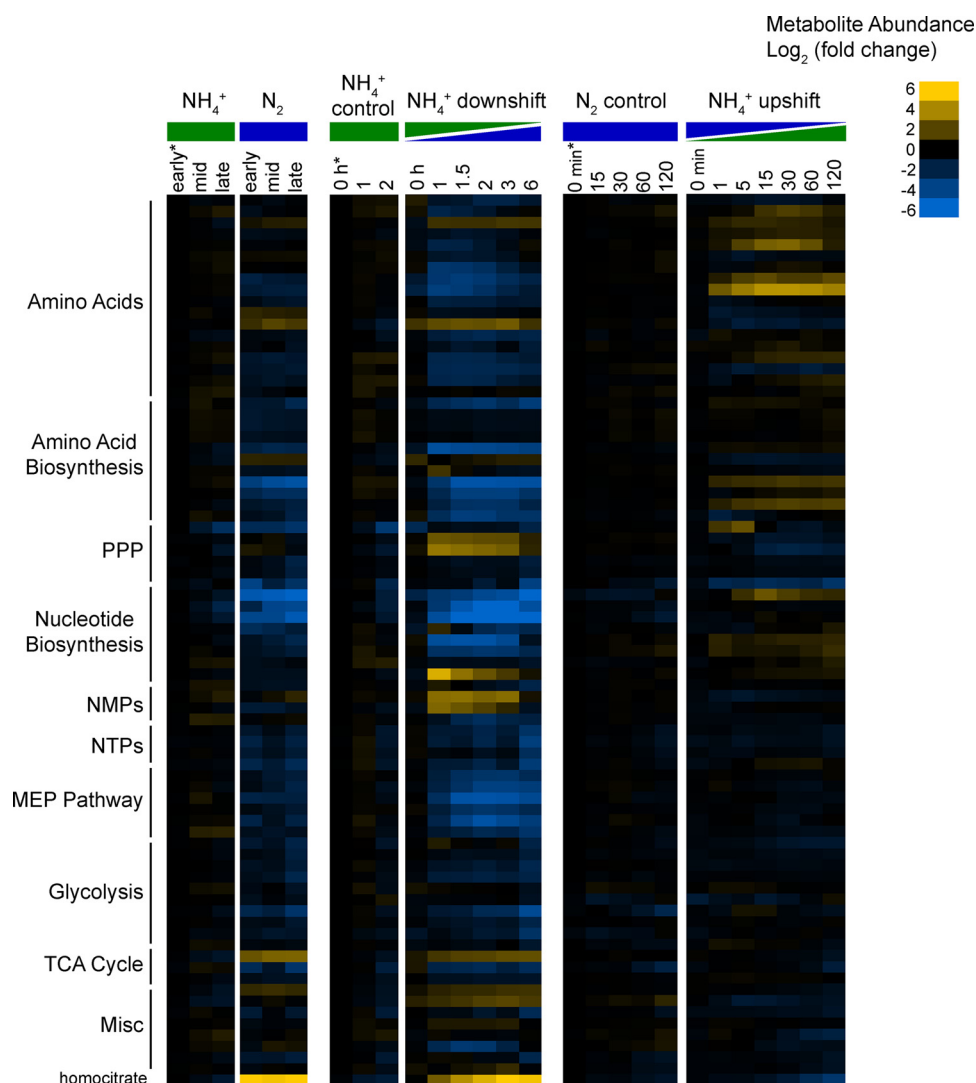
We examined three separate regimes of nitrogen availability (Fig. 1A). (i) Continuous  $\text{N}_2$ -fixing conditions were compared to continuous  $\text{NH}_4^+$ -replete conditions; doubling times were approximately 3 h during  $\text{N}_2$  fixation and 2 h under  $\text{NH}_4^+$ -replete conditions (Fig. 1B). Samples were taken for targeted metabolomics at early, mid-, and late exponential phase and for shotgun proteomics at mid-exponential phase. (ii)  $\text{NH}_4^+$  downshift; *Z. mobilis* was grown in medium containing limited  $\text{NH}_4^+$  (<2 mM) such that growth stalled at mid-exponential phase. During the dynamic shift to  $\text{N}_2$  fixation, a 6-h metabolomics and proteomics time course was conducted. Samples were collected for the initial ( $t = 0$ ) time point during early exponential



**FIG 1** (A) Schematic of experimental design. See Materials and Methods for more details. (B to D) Representative growth of *Z. mobilis* cultures measured by optical density at 600 nm. (B) Continuous N<sub>2</sub>-fixing conditions (blue squares) compared to continuous NH<sub>4</sub><sup>+</sup>-replete conditions (15 mM NH<sub>4</sub><sup>+</sup>) (green circles). Times of metabolite extractions are shown as red symbols. Protein extractions were conducted at an OD<sub>600</sub> of ~0.5. Data points are the average of 3 biological replicates. Error bars showing standard deviation are smaller than the height of symbols. (C) Replete (15 mM) NH<sub>4</sub><sup>+</sup> controls (green circles) compared to NH<sub>4</sub><sup>+</sup> downshift (starting with <5 mM NH<sub>4</sub><sup>+</sup>) (blue squares). Arrows indicate start and end of time course. Times of metabolite and protein extraction are shown as red symbols. Data points are the average of 3 biological replicates for NH<sub>4</sub><sup>+</sup> downshift and 2 biological replicates for controls. Error bars showing standard deviation are smaller than the height of the symbols. (D) Continuous N<sub>2</sub>-fixing controls (blue squares) compared to NH<sub>4</sub><sup>+</sup> upshift (15 mM NH<sub>4</sub>Cl was added to N<sub>2</sub>-fixing cultures at t = 0) (green circles). Arrows and red symbols indicate metabolite and protein extractions taken at start and end of time course. See Materials and Methods for a full list of time points within this time course. Data points are the average of 3 biological replicates for NH<sub>4</sub><sup>+</sup> upshift and 2 biological replicates for controls. Error bars show the standard deviation.

growth before a decrease in growth rate was observed, i.e., when the doubling time was still ~2 h (Fig. 1C). Samples were also taken from NH<sub>4</sub><sup>+</sup>-replete controls which grew with a doubling time of 2 h (Fig. 1C). (iii) NH<sub>4</sub><sup>+</sup> upshift; *Z. mobilis* was grown under N<sub>2</sub>-fixing conditions until early exponential phase, at which point NH<sub>4</sub>Cl was added to the medium at a final concentration of 15 mM. During NH<sub>4</sub><sup>+</sup> upshift, a 2-h metabolomics and proteomics time course was conducted. Samples were collected for the initial (t = 0) time point immediately before addition of NH<sub>4</sub>Cl. Samples were also taken from N<sub>2</sub>-fixing controls. Both conditions grew with a consistent 3-h doubling time for the duration of the 2-h time course (Fig. 1D).

**Metabolome analysis reveals global alterations in intracellular metabolite levels in response to changes in nitrogen availability.** Metabolomic analysis using LC-MS produced relative intracellular abundance for 99 unique metabolites spanning central carbon metabolism (see Table S1 in the supplemental material). These included intermediates of Entner-Doudoroff (ED) glycolysis, the pentose phosphate pathway (PPP), the tricarboxylic acid (TCA) cycle, amino acid biosynthesis, nucleotide biosynthesis, isoprenoid biosynthesis, and peptidoglycan biosynthesis. Of the 99 detected metabolites, 79 were differentially abundant (fold change [FC] of >1.5 and false discovery rate [FDR]-adjusted *P* value of <0.05) during at least one of the three conditions of nitrogen availability (Fig. 2). In general, amino acids and intermediates in amino acid biosynthesis were depleted during N<sub>2</sub> fixation and either increased or remained constant in response to NH<sub>4</sub><sup>+</sup> upshift. One notable exception was arginine, which increased during N<sub>2</sub> fixation and decreased after NH<sub>4</sub><sup>+</sup> addition. Intermediates of *de novo* nucleotide biosynthesis were severely depleted (>30-fold decrease) under N<sub>2</sub>-



**FIG 2** Relative intracellular metabolite abundance of the 79 metabolites that were differentially abundant (fold change of  $\geq 1.5$  and FDR-adjusted  $P$  value of  $\leq 0.05$ ) during at least one of the three conditions of nitrogen availability; from left to right, continuous NH<sub>4</sub><sup>+</sup>-replete conditions versus continuous N<sub>2</sub>-fixing conditions, NH<sub>4</sub><sup>+</sup> downshift (shift to N<sub>2</sub>-fixing conditions), and NH<sub>4</sub><sup>+</sup> upshift (from N<sub>2</sub>-fixing conditions), respectively. Rows are a single metabolite across all conditions, and columns are individual metabolomics samples, taken at the indicated times and conditions. Log<sub>2</sub> fold changes are relative to the first time point in the control condition for each experiment (indicated by an asterisk). Values are the averages of 2 biological replicates for time course controls, 3 biological replicates for time course treatments, and 5 biological replicates for both continuous conditions. Yellow corresponds to increased intracellular metabolite abundance compared to the control, and blue indicates depletion. Metabolites were manually arranged based on the biosynthetic pathway.

fixing conditions. Nucleotide triphosphates (NTPs) were also less abundant during N<sub>2</sub> fixation, although to a lesser extent ( $\sim 4$ -fold decrease). Conversely, intracellular concentrations of nucleosides and nucleotide monophosphates (NMPs) increased during the shift to N<sub>2</sub> fixation. There were dynamic changes in the PPP during shifts in NH<sub>4</sub><sup>+</sup> availability, which are likely linked to nucleotide biosynthesis. We observed depletion of intermediates in both the ED glycolytic pathway and the methylerythritol phosphate (MEP) pathway for isoprenoid biosynthesis during N<sub>2</sub> fixation. Overall, intracellular metabolite levels changed dramatically during the shift to N<sub>2</sub> fixation but remained much more consistent during NH<sub>4</sub><sup>+</sup> upshift, where the largest changes corresponded to increased amino acid abundance, particularly glutamine.

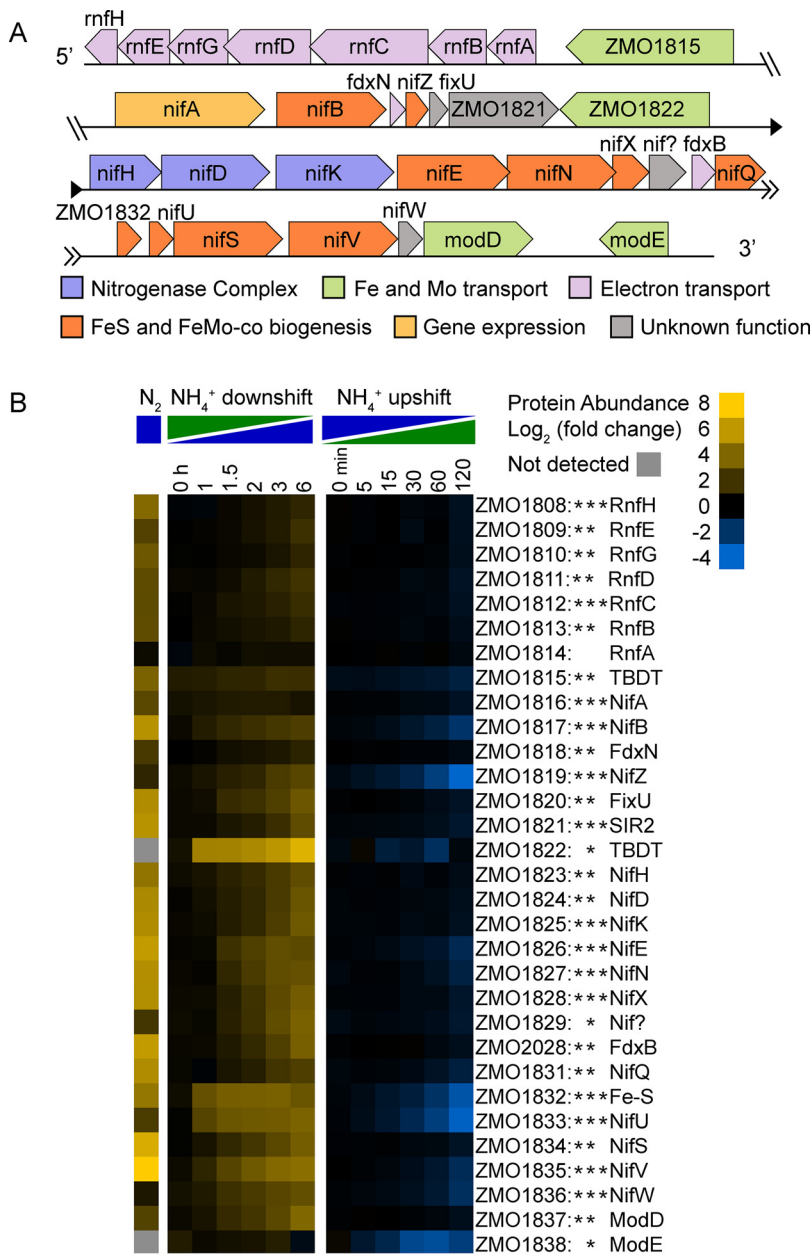
**Proteome remodeling in response to changes in nitrogen availability.** Proteomics analysis during NH<sub>4</sub><sup>+</sup> downshift and NH<sub>4</sub><sup>+</sup> upshift produced relative protein abundance for

1,693 unique proteins (90% coverage of protein coding genes) (22, 25, 26). The comparison between continuous N<sub>2</sub> and NH<sub>4</sub><sup>+</sup> growth conditions was performed separately and yielded 1,429 proteins (75% coverage). Of the proteins detected, 615 changed significantly during at least one of the three conditions of N<sub>2</sub> availability (FC of >1.5 and FDR-adjusted *P* value of <0.05) (Table S2). We identified 296 proteins that were affected during continuous N<sub>2</sub> fixation relative to continuous replete NH<sub>4</sub><sup>+</sup>, 467 proteins that were differentially abundant during the shift to N<sub>2</sub> fixation, and only 33 proteins that responded to the NH<sub>4</sub><sup>+</sup> upshift. We performed an overrepresentation analysis of gene ontology (GO) terms associated with the set of proteins found to be differentially abundant under each of the three conditions (Table S3) (27). All three conditions yielded “nitrogen fixation,” “nitrogenase activity,” and “iron-sulfur cluster binding” as terms that were enriched among affected proteins. Proteins that were differentially abundant during the N<sub>2</sub> versus NH<sub>4</sub><sup>+</sup> conditions were also enriched for “regulation of nitrogen utilization,” “cellular iron ion homeostasis,” “cysteine desulfurase activity,” and “arginine biosynthetic process via ornithine” among other terms. Proteins that changed in abundance during NH<sub>4</sub><sup>+</sup> downshift were also enriched for GO terms such as “siderophore uptake transmembrane transporter activity,” “bacterial-type flagellum,” “oxidoreductase activity,” and “response to oxidative stress.” Products of the nitrogen fixation (*nif*) gene cluster were consistently among the most affected proteins under all three conditions of NH<sub>4</sub><sup>+</sup> availability (Fig. 3). During the transition to N<sub>2</sub> fixation, proteins involved in metal transport, electron transport, and oxidative stress increased in abundance, whereas proteins involved in translation and motility decreased in abundance (Fig. S1 and S2). Our integrated metabolomics and proteomics analysis in *Z. mobilis* also revealed widespread and dynamic remodeling of metabolism in response to changes in nitrogen availability. In the following sections, we summarize a subset of the most significant alterations.

**Concerted increase in the abundance of nitrogenase and nitrogenase-supporting enzymes during N<sub>2</sub>-fixing conditions.** In *Z. mobilis*, as in other nitrogen-fixing bacteria, the genes required for N<sub>2</sub> fixation are clustered within a 30-kb genomic region called the *nif* cluster (28, 29). The *Z. mobilis* *nif* cluster contains 31 genes: *nifABZHDKENXQUSVW*, *fdxN*, *fixU*, *fdxB*, *modD*, *modE*, the *rnfABCDGEH* operon, a gene (ZMO1832) encoding an iron-sulfur cluster assembly accessory protein, two genes (ZMO1815 and ZMO1822) encoding iron-associated TonB-dependent transporters (TBDT), an uncharacterized N<sub>2</sub> fixation gene (ZMO1829), and a gene (ZMO1821) encoding a hypothetical protein with an SIR2-like domain (30) (Fig. 3A). The *nif* cluster codes for the three proteins that form the active nitrogenase complex: nitrogenase reductase (NifH), also called the Fe protein, and the  $\alpha$  and  $\beta$  subunits of nitrogenase (NifD and NifK), also called the MoFe protein. Several genes in the *nif* cluster (e.g., *nifB*, *nifU*, *nifE*, *nifN*, and *nifV*) are involved in the biogenesis of iron-sulfur clusters required for N<sub>2</sub> fixation, including the [Fe<sub>4</sub>-S<sub>4</sub>] cluster cofactor of NifH, the [Fe<sub>8</sub>-S<sub>7</sub>] cluster (P-cluster) cofactor of NifDK, and the [Mo-Fe<sub>7</sub>-S<sub>9</sub>-C-homocitrate] molybdenum-iron cofactor (FeMo-co) at the active site of NifDK (31, 32). The *nif* gene cluster also contains the *rnf* operon, whose products form a membrane-bound complex that couples ion translocation across the inner membrane to the transfer of electrons from NADH to ferredoxin (e.g., FdxN or FdxB), which then donates electrons to the nitrogenase complex (33, 34). The *nif* cluster is regulated by the  $\sigma^{54}$ -dependent transcription factor NifA, which is also encoded within the *nif* cluster (35–39).

Our proteomics analysis revealed a concerted increase in abundance of *nif* cluster proteins during N<sub>2</sub>-fixing conditions (Fig. 3B). Under continuous N<sub>2</sub>-fixing conditions, 27 out of 29 detected *nif* cluster proteins were significantly elevated (FC > 1.5, FDR < 0.05) (Fig. 3B). Levels of nitrogenase proteins NifH, NifD, and NifK were elevated by 23-fold, 41-fold, and 46-fold, respectively, during continuous N<sub>2</sub> fixation (Fig. 4A). During the dynamic shift to N<sub>2</sub>-fixing conditions, 30 out of 31 *nif* cluster proteins increased significantly in abundance (Fig. 3B). Levels of NifH, NifD, and NifK were elevated by 2-fold above the NH<sub>4</sub><sup>+</sup>-replete baseline after 1.5 h (just as growth stalled) and by over 8-fold after 6 h (Fig. 4A).

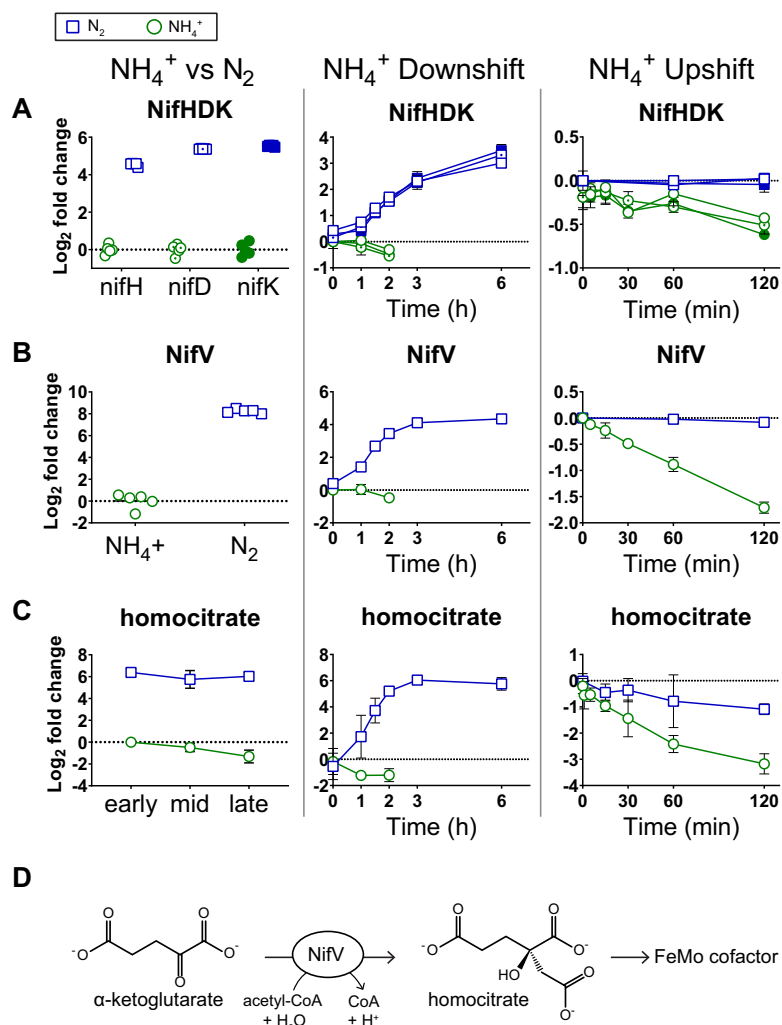
One of most affected proteins from the *nif* cluster was homocitrate synthase (NifV), which was 300-fold more abundant during continuous N<sub>2</sub> fixation and increased by 16-



**FIG 3** (A) Schematic of the *nif* gene cluster in *Z. mobilis*. For each gene, the arrow length is representative of the approximate length of the coding region and the arrow direction corresponds to the direction of transcription. Colors were assigned based on gene function. (B) Relative protein abundance of gene products from the *nif* cluster. Log<sub>2</sub> fold changes are relative to the first time point in the control condition (not shown). Values are the averages of at least 3 biological replicates. Asterisks indicate statistical significance (FC ≥ 1.5, FDR ≤ 0.05) for NH<sub>4</sub><sup>+</sup> versus N<sub>2</sub>, NH<sub>4</sub><sup>+</sup> downshift, and NH<sub>4</sub><sup>+</sup> upshift experiments, respectively, from left to right. For example, RnfH protein abundance changed significantly for all three conditions, but changes in RnfE abundance were only significant for NH<sub>4</sub><sup>+</sup> versus N<sub>2</sub> and NH<sub>4</sub><sup>+</sup> downshift conditions. A gray tile indicates that protein was not detected under that condition. Proteins were manually arranged based on genomic location within the *nif* cluster.

fold during the shift to N<sub>2</sub>-fixing conditions (Fig. 4B). NifV transfers an acetyl group from acetyl coenzyme A (acetyl-CoA) to α-ketoglutarate to produce homocitrate, which chelates the Mo atom in the FeMo-co at the active site of nitrogenase (Fig. 4D) (40, 41). Metabolomics analysis showed that intracellular homocitrate levels increased by over 60-fold during N<sub>2</sub> fixation (both continuous N<sub>2</sub> fixation and transition to N<sub>2</sub> fixation), which was the largest increase in metabolite abundance observed in this study (Fig. 2 and 4C).





**FIG 4** Relative abundance of proteins and metabolites related to nitrogenase function during three conditions of nitrogen availability. Blue squares indicate N<sub>2</sub> fixation or transition to N<sub>2</sub> fixation. Green circles indicate replete NH<sub>4</sub><sup>+</sup> or NH<sub>4</sub><sup>+</sup> upshift. Log<sub>2</sub> fold change values are relative to the first time point in the control condition. For NH<sub>4</sub><sup>+</sup> versus N<sub>2</sub> protein abundance, individual data points are shown (5 biological replicates per condition). For all other graphs, values are the average of at least 3 biological replicates for the treatment condition and at least 2 biological replicates for controls. Error bars show standard deviations (SD). (A) Protein abundance of nitrogenase structural proteins, including Fe protein (NifH) (open symbols), α subunit of MoFe protein (NifD) (open symbols with dots), and β subunit of MoFe protein (NifK) (closed symbols). (B) Protein abundance of homocitrate synthase (NifV). (C) Intracellular metabolite abundance of homocitrate. (D) Reaction catalyzed by homocitrate synthase. Homocitrate is then incorporated into the FeMo cofactor as a bidentate chelator of Mo.

During NH<sub>4</sub><sup>+</sup> upshift, fewer changes in *nif* cluster protein abundance occurred (Fig. 3B). Only 14 of the 31 *nif* cluster proteins decreased significantly relative to N<sub>2</sub>-fixing controls. The largest decreases were in NifZ, NifU, NifB, NifW, NifV, NifE, NifN, and the iron-sulfur cluster assembly accessory protein ZMO1832, all of which decreased by over 2-fold (Fig. 3B and 4B). Given that less than one cell doubling occurred during the NH<sub>4</sub><sup>+</sup> upshift time course experiment, decreases over 2-fold imply active protein degradation rather than dilution by cell division. Many of the proteins that decreased in abundance are involved in the biogenesis of FeS or FeMo cofactors, including NifV, whose depletion coincided with an 8-fold drop in intracellular levels of homocitrate (Fig. 4C). Protein levels of nitrogenase proteins NifH, NifD, and NifK all showed decreasing trends during NH<sub>4</sub><sup>+</sup> upshift, but only NifK met our criteria (FC > 1.5, FDR < 0.05) for differential expression and all three remained within 2-fold of the N<sub>2</sub>-fixing baseline

(Fig. 4A). Together, these results suggest that biogenesis of FeS and FeMo cofactors is rapidly repressed via protein degradation during an acute increase in  $\text{NH}_4^+$  availability, even while NifHDK protein abundance remains relatively constant. Delaying degradation of nitrogenase may provide a fitness advantage in environments where bioavailable nitrogen is transiently available. Modulation of iron-sulfur cluster biogenesis and intracellular homocitrate levels may contribute to the regulation of nitrogenase activity during changes in  $\text{NH}_4^+$  availability.

#### Decreased abundance of flagellar and chemotaxis proteins during $\text{N}_2$ fixation.

In the *Z. mobilis* genome, the genes involved in flagellar motility (ZMO0602-ZMO0652) and several genes related to chemotaxis signal transduction (ZMO0078-ZMO0085) are each organized within their own gene cluster (30, 42). Several flagellar proteins (FlgL, FlgK, FlgI, FlgD, FlgC, FlgB, FlIF, FlII, FlIK, FlIO, FlID, and FlIK) and chemotaxis proteins (CheY, CheD, CheA, and CheX) from these two gene clusters were significantly depleted ( $\text{FC} > 1.5$ ,  $\text{FDR} < 0.05$ ) during the transition to  $\text{N}_2$ -fixing conditions (Fig. S2). Decreases in abundance of motility proteins was seen as early as 1 h into the  $\text{NH}_4^+$  downshift. FlgI, FlIF, FlII, CheR, CheA, and McpJ were also less abundant during continuous  $\text{N}_2$ -fixing conditions ( $\text{FC} > 1.5$ ,  $\text{FDR} < 0.05$ ). No significant trends were observed in proteins from either gene cluster in response to  $\text{NH}_4^+$  upshift.

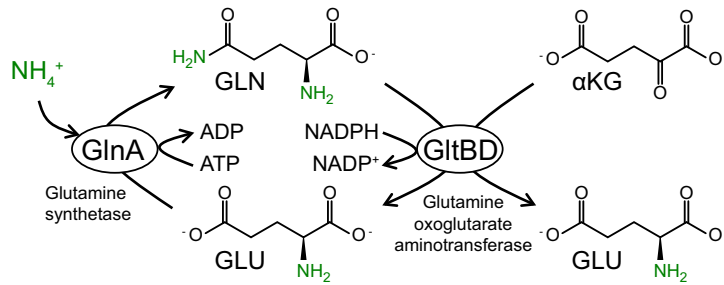
Bacterial flagellar motors are powered by the translocation of ions across the inner membrane (43, 44). Others have observed decreased expression of flagellar genes in *Z. mobilis* under stress conditions that disrupt the maintenance of an electrochemical gradient across the membrane, such as low pH, osmotic stress, and high ethanol concentrations (45–47). This is in contrast to other environmental inhibitors such as oxygen and lignocellulosic toxins, which have been shown to increase expression of motility-related genes in *Z. mobilis* (48–50). Previous transcriptomics analysis of *Z. mobilis* both during adaptation to high glucose concentrations and in the presence of a quorum sensing autoinducer each showed that expression of flagellar genes decreased concomitantly with increased expression of genes from the *nif* cluster (20, 46). Given that the Rnf complex utilizes energy stored in the electrochemical gradient to drive production of reduced ferredoxin (the electron donor to nitrogenase reductase), decreased expression of flagellar proteins (and, presumably, decreased energy consumption by the flagellar motor) may be important for maintaining a robust electrochemical gradient during  $\text{N}_2$ -fixing conditions.

**Dynamics of  $\text{NH}_4^+$  assimilation via the GS-GOGAT cycle.** There are two major pathways for  $\text{NH}_4^+$  assimilation in bacteria (51). One of these pathways is comprised of glutamine synthetase (GS) and glutamine oxoglutarate aminotransferase (GOGAT), which together form the GS-GOGAT cycle (Fig. 5A). In this pathway, GS catalyzes the condensation of glutamate and ammonia to form glutamine, converting one molecule of ATP to ADP in the process (52). Next, GOGAT transfers the amino group from glutamine to  $\alpha$ -ketoglutarate ( $\alpha$ KG), forming two molecules of glutamate and converting one molecule of NAD(P)H to NAD(P)<sup>+</sup> (53). The other bacterial route for ammonia assimilation is via glutamate dehydrogenase (GDH), which directly converts  $\alpha$ KG to glutamate by reductive amination of  $\alpha$ KG, also consuming one molecule of NAD(P)H (54). The two pathways differ in their energy (ATP) consumption and affinity for  $\text{NH}_4^+$  (54–56). In *Escherichia coli*, it is generally understood that the GS-GOGAT cycle is employed during low  $\text{NH}_4^+$  availability while GDH is active during high  $\text{NH}_4^+$  availability or energy limitation (56, 57). In *Z. mobilis*, no *gdh* gene has been identified based on sequence homology (58). However, genes encoding GS (*glnA*) and the large and small subunits of GOGAT (*gltB* and *gltD*) have been annotated (30) (Fig. 5A).

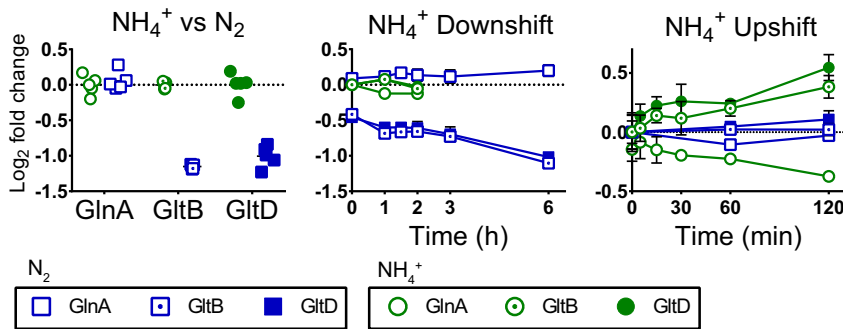
Proteomics analysis determined relative abundance of GS (GlnA) and the large and small subunits of GOGAT (GltB and GltD) during continuous  $\text{N}_2$  fixation,  $\text{NH}_4^+$  downshift, and  $\text{NH}_4^+$  upshift (Fig. 5B). Interestingly, GS levels did not change significantly for any of the three conditions of  $\text{NH}_4^+$  availability ( $\text{FC} < 1.3$ ,  $\text{FDR} > 0.2$ ) (Fig. 5B). However, both subunits of GOGAT were 2-fold lower during continuous  $\text{N}_2$  fixation than during  $\text{NH}_4^+$ -replete conditions (Fig. 5B). During  $\text{NH}_4^+$  downshift, GOGAT levels were already lower than in  $\text{NH}_4^+$ -replete controls at the initial time point (before changes in growth rate were observed), and they continued to fall for the duration of



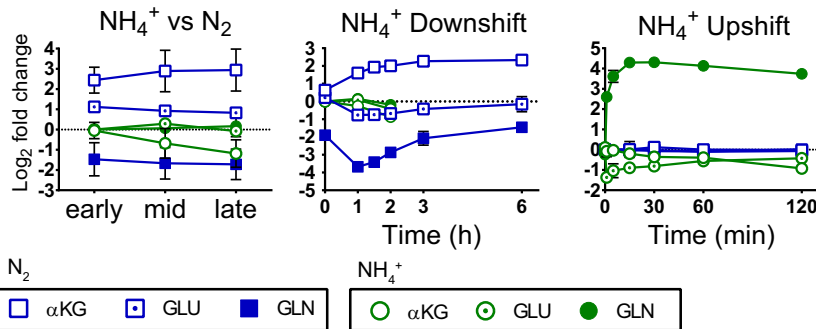
## A The GS-GOGAT cycle



## B Protein Abundance: GS-GOGAT enzymes



## C Metabolite Abundance: GS-GOGAT intermediates



**FIG 5** (A) Schematic of the GS-GOGAT cycle. (B and C) Relative abundance of proteins (B) and metabolites (C) in the GS-GOGAT cycle during three conditions of nitrogen availability. Blue squares indicate N<sub>2</sub> fixation or transition to N<sub>2</sub> fixation. Green circles indicate replete NH<sub>4</sub><sup>+</sup> or NH<sub>4</sub><sup>+</sup> upshift. Log<sub>2</sub> fold change values are relative to the first time point in the control condition. For NH<sub>4</sub><sup>+</sup> versus N<sub>2</sub> protein abundance, individual data points are shown (5 biological replicates per condition). For all other graphs, values are the average of at least 3 biological replicates for the treatment condition and at least 2 biological replicates for controls. Error bars show SD. (B) Protein abundance of glutamine synthetase (GlnA) (open symbols), the  $\alpha$  (large) subunit of glutamine oxoglutarate aminotransferase (GltB) (open symbols with dots), and the  $\beta$  (small) subunit of GOGAT (GltD) (closed symbols). (C) Metabolite abundance of  $\alpha$ -ketoglutarate (open symbols), glutamate (open symbols with dots), and glutamine (closed symbols).

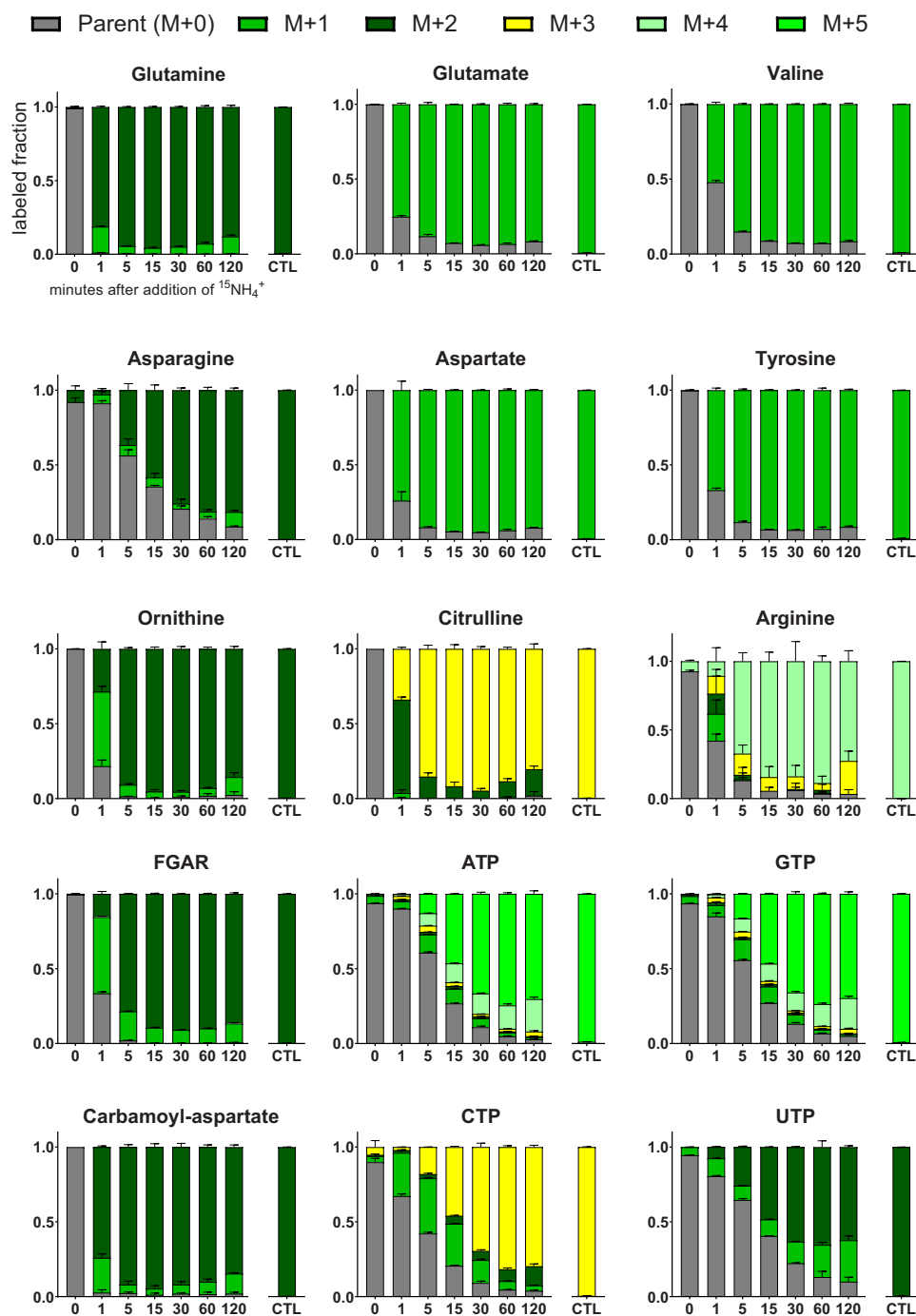
the NH<sub>4</sub><sup>+</sup> downshift time course, reaching 2-fold below controls at the 6-h time point (Fig. 5C). There was an increasing trend for both subunits of GOGAT during NH<sub>4</sub><sup>+</sup> upshift (FDR = 0.072 and 0.029, respectively), but levels remained within 1.5-fold of controls (Fig. 5B). Overall, GS enzyme levels remained constant and GOGAT enzymes levels decreased during N<sub>2</sub> fixation. Regulation of GS via posttranslational adenylation by GS adenylyltransferase/adenylyl-removing enzyme (AT/AR) is common in other proteobacteria (59). However, no AT/AR gene has been annotated in the *Z. mobilis* genome. On the other hand, differential phosphorylation of both GS and GOGAT have been observed during N<sub>2</sub> fixation in *Z. mobilis*, likely contributing to the regulation of GS-GOGAT cycle activity (60).

Metabolomics analysis produced relative intracellular abundance of glutamine, glutamate, and  $\alpha$ KG during the three conditions of  $\text{NH}_4^+$  availability (Fig. 5C). Under continuous  $\text{N}_2$ -fixing conditions, intracellular glutamine levels were 3-fold lower, glutamate levels were 2-fold higher, and  $\alpha$ KG levels were 8-fold higher than under  $\text{NH}_4^+$ -replete conditions (Fig. 5C). During  $\text{NH}_4^+$  downshift, glutamine levels were already 3-fold lower than those of  $\text{NH}_4^+$ -replete controls at the initial time point and dropped to 12-fold below controls after 1 h, when growth began to stall. From the 1-h time point to the 6-h time point, intracellular glutamine levels rose, tracking with the rise in nitrogenase protein levels (Fig. 5C and 4A). Glutamate levels remained within 2-fold of control levels for the entire downshift time course but matched the trends seen in glutamine, dropping in the first hour and then increasing from 1 to 6 h. Levels of  $\alpha$ KG increased for the duration of the downshift time course, reaching 5-fold above baseline after 6 h (Fig. 5C).

During  $\text{NH}_4^+$  upshift, intracellular glutamine levels immediately increased, reaching 6-fold above the  $\text{N}_2$ -fixing control within 1 min of  $\text{NH}_4^+$  addition. Glutamine levels continued to rise for 30 min following  $\text{NH}_4^+$  addition, reaching 20-fold above baseline before gradually decreasing to 13-fold above baseline by the 2-h time point. Glutamate levels trended in the opposite direction, first dropping to 2.5-fold below  $\text{N}_2$ -fixing controls within 1 min and then increasing for the remainder of the time course, ending within 1.5-fold of the controls.  $\alpha$ KG levels did not change within the first 15 min of the  $\text{NH}_4^+$  upshift time course but decreased by around 2-fold from 15 min to 2 h (Fig. 5C).

Previous studies in *E. coli* and *Rhodospirillum rubrum* have found that upon addition of  $\text{NH}_4^+$  to nitrogen-limited cultures, intracellular glutamine levels increased rapidly but then quickly declined within 5 to 10 min (61, 62). The decline in glutamine levels following their accumulation was associated with fast inactivation of GS via adenylylation by AT/AR (61, 63, 64). In *Z. mobilis*, glutamine levels rapidly increased following  $\text{NH}_4^+$  upshift but did not decline in the first 30 min and remained substantially elevated compared to steady-state levels for over 2 h, suggesting that GS activity is not rapidly inhibited in response to increased  $\text{NH}_4^+$  availability. The fact that the *Z. mobilis* genome apparently does not encode AT/AR may help explain the persistence of elevated glutamine levels following  $\text{NH}_4^+$  addition in *Z. mobilis*. More research should be conducted to investigate the regulatory mechanisms that control GS activity in *Z. mobilis*, as they appear to be distinct from the classical model that has been well studied in other proteobacteria (65, 66).

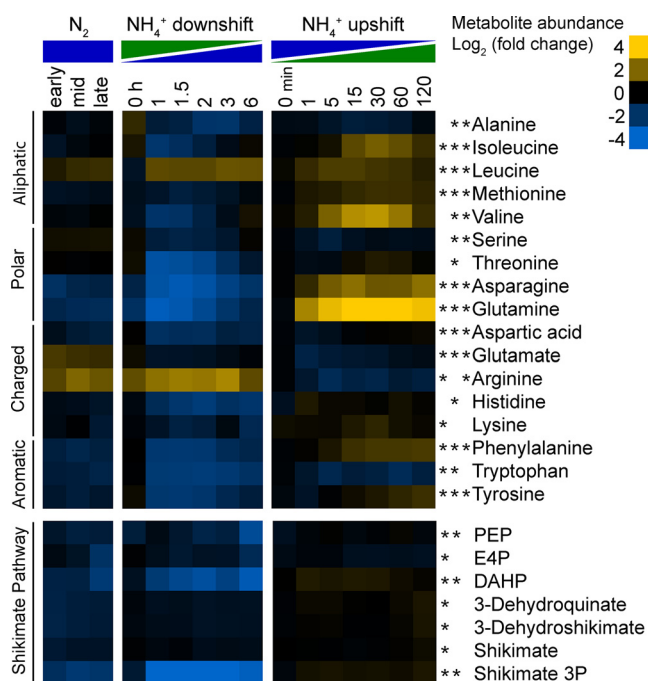
**Addition of  $^{15}\text{NH}_4^+$  to  $\text{N}_2$ -fixing cultures shows immediate assimilation of exogenous  $\text{NH}_4^+$  and possible residual nitrogenase activity.** The immediate increase in intracellular glutamine levels following  $\text{NH}_4^+$  addition indicates that *Z. mobilis* is poised to rapidly incorporate exogenous  $\text{NH}_4^+$  as soon as it becomes available, even in an  $\text{N}_2$ -fixing state. This was expected given that  $\text{NH}_4^+$  is a product of nitrogenase, and at high (mM) extracellular concentrations,  $\text{NH}_4^+$  can passively diffuse across the membrane to support growth in other bacteria (67). To examine the dynamics of  $\text{NH}_4^+$  assimilation and incorporation more closely, we performed a separate iteration of the  $\text{NH}_4^+$  upshift experiment using  $^{15}\text{NH}_4\text{Cl}$  (see Materials and Methods). This allowed us to trace the incorporation of exogenous  $\text{NH}_4^+$  into metabolite pools, providing insight into the turnover rate of nitrogen-containing metabolites during  $\text{NH}_4^+$  upshift (Fig. 6). Within 1 min after addition of  $^{15}\text{NH}_4^+$ , glutamine levels were 99%  $^{15}\text{N}$  labeled (i.e., containing at least one  $^{15}\text{N}$  atom). Similar trends were observed for glutamate, which was 90%  $^{15}\text{N}$  labeled after 5 min. Most amino acids followed these trends, with a few exceptions. Most notably, asparagine labeled much more slowly and was still over 50% unlabeled after 5 min. This suggests that either rates of asparagine biosynthesis are low compared to other amino acids, intracellular pools of asparagine are high compared to other amino acids, or there is some compartmentalized pool of asparagine (e.g., periplasmic or extracellular) that is subject to a lower turnover rate. The rate of  $^{15}\text{N}$  incorporation into nucleotide biosynthetic intermediates was similar to that of glutamine and glutamate, showing that exogenously supplied  $\text{NH}_4^+$  was rapidly utilized for *de novo* synthesis of both purines and pyrimidines. Nucleotide triphosphates such as ATP



**FIG 6** Dynamics of metabolite labeling patterns following addition of  $^{15}\text{NH}_4^+$  to N<sub>2</sub>-fixing cultures (15 mM final concentration) compared to controls (CTL) that were grown with 15 mM  $^{15}\text{NH}_4^+$  continuously. The y axis represents the relative proportion of each labeled form at each time point. Values are the average of 3 biological replicates. Error bars show SD. M + 1 indicates the presence of one  $^{15}\text{N}$  nitrogen atom in the molecule, M + 2 indicates the presence of two  $^{15}\text{N}$  nitrogen atoms, etc. M + 0 indicates that all nitrogen atoms are  $^{14}\text{N}$ . Masses were adjusted to account for the natural abundance of  $^{15}\text{N}$  (see Materials and Methods). Abbreviation: FGAR, phosphoribosyl-*N*-formylglycineamide.

labeled more slowly than their upstream intermediates, as would be expected, but after 2 h, less than 5% of the NTP pool remained unlabeled.

Interestingly, from 15 min to 2 h, we observed a small but significant ( $P < 0.01$ ) loss of  $^{15}\text{N}$  label in glutamine. The fully labeled fraction (i.e., containing two  $^{15}\text{N}$  atoms) of glutamine went from 95% after 15 min to 88% after 2 h, implying increasing



**FIG 7** Relative intracellular metabolite abundance of amino acids and intermediates in aromatic amino acid biosynthesis. Log<sub>2</sub> fold change values are relative to the first time point in the control condition (not shown). Values are the averages of at least 3 biological replicates. Asterisks indicate statistical significance (FC  $\geq$  1.5, FDR  $\leq$  0.05) for NH<sub>4</sub><sup>+</sup> versus N<sub>2</sub>, NH<sub>4</sub><sup>+</sup> downshift, and NH<sub>4</sub><sup>+</sup> upshift conditions, respectively, from left to right. For example, intracellular levels of alanine changed significantly during NH<sub>4</sub><sup>+</sup> downshift and NH<sub>4</sub><sup>+</sup> upshift but not during continuous NH<sub>4</sub><sup>+</sup> versus N<sub>2</sub> conditions. Metabolites were manually arranged based on chemical properties of the side chain for amino acids and by metabolic pathway order for the shikimate pathway. Abbreviations: PEP, phosphoenolpyruvate; E4P, erythrose 4-phosphate; DAHP, 2-dehydro-3-deoxy-D-arabino-heptonate 7-phosphate.

assimilation of unlabeled (<sup>14</sup>N) nitrogen. Loss of <sup>15</sup>N label was also seen in other metabolites, including intermediates in amino acid and nucleotide biosynthesis. This loss of <sup>15</sup>N label might be the result of protein degradation, which could liberate amino acids and NH<sub>4</sub><sup>+</sup> from proteins that had been translated during <sup>14</sup>N<sub>2</sub> fixation. However, given the observation that nitrogenase protein levels did not decrease by more than 2-fold during NH<sub>4</sub><sup>+</sup> upshift, loss of <sup>15</sup>N label could also be caused by residual nitrogenase activity following increased availability of NH<sub>4</sub><sup>+</sup>. In some diazotrophic alphaproteobacteria (e.g., *R. rubrum*), NH<sub>4</sub><sup>+</sup> upshift induces rapid but reversible inactivation of NifH via ADP-ribosylation by DraT/DraG (68–70). However, neither *draT* nor *draG* homologues have been identified in the *Z. mobilis* genome. Control samples extracted from cells grown with replete <sup>15</sup>NH<sub>4</sub><sup>+</sup> for over 6 generations were >99% fully <sup>15</sup>N labeled for all nitrogen-containing metabolites detected (Fig. 6). This indicates that long-term replete NH<sub>4</sub><sup>+</sup> availability does result in complete repression of nitrogenase activity.

**Effect of nitrogen availability on amino acid abundance.** We measured the relative intracellular abundance of 17 amino acids (Fig. 7). Levels of glutamine, asparagine, aspartic acid, isoleucine, methionine, lysine, and aromatic amino acids (phenylalanine, tryptophan, and tyrosine) were all significantly depleted (FC > 1.5, FDR < 0.05) during N<sub>2</sub> fixation compared to NH<sub>4</sub><sup>+</sup>-replete conditions. Glutamate, leucine, and arginine were the only amino acids whose levels were significantly elevated during continuous N<sub>2</sub> fixation. During the dynamic shift to N<sub>2</sub> fixation, all measured amino acids other than lysine, arginine, and leucine decreased significantly. Leucine and arginine levels both increased by over 3-fold, but lysine did not display any significant trends. During NH<sub>4</sub><sup>+</sup> upshift, the largest change in amino acid abundance was the 20-fold increase in glutamine levels, but asparagine, isoleucine, leucine, valine, methionine, tyrosine, and phenylalanine levels also increased significantly compared to the N<sub>2</sub>-fixing control.

Abundance of glutamate, arginine, alanine, serine, and aspartic acid all decreased significantly during the NH<sub>4</sub><sup>+</sup> upshift.

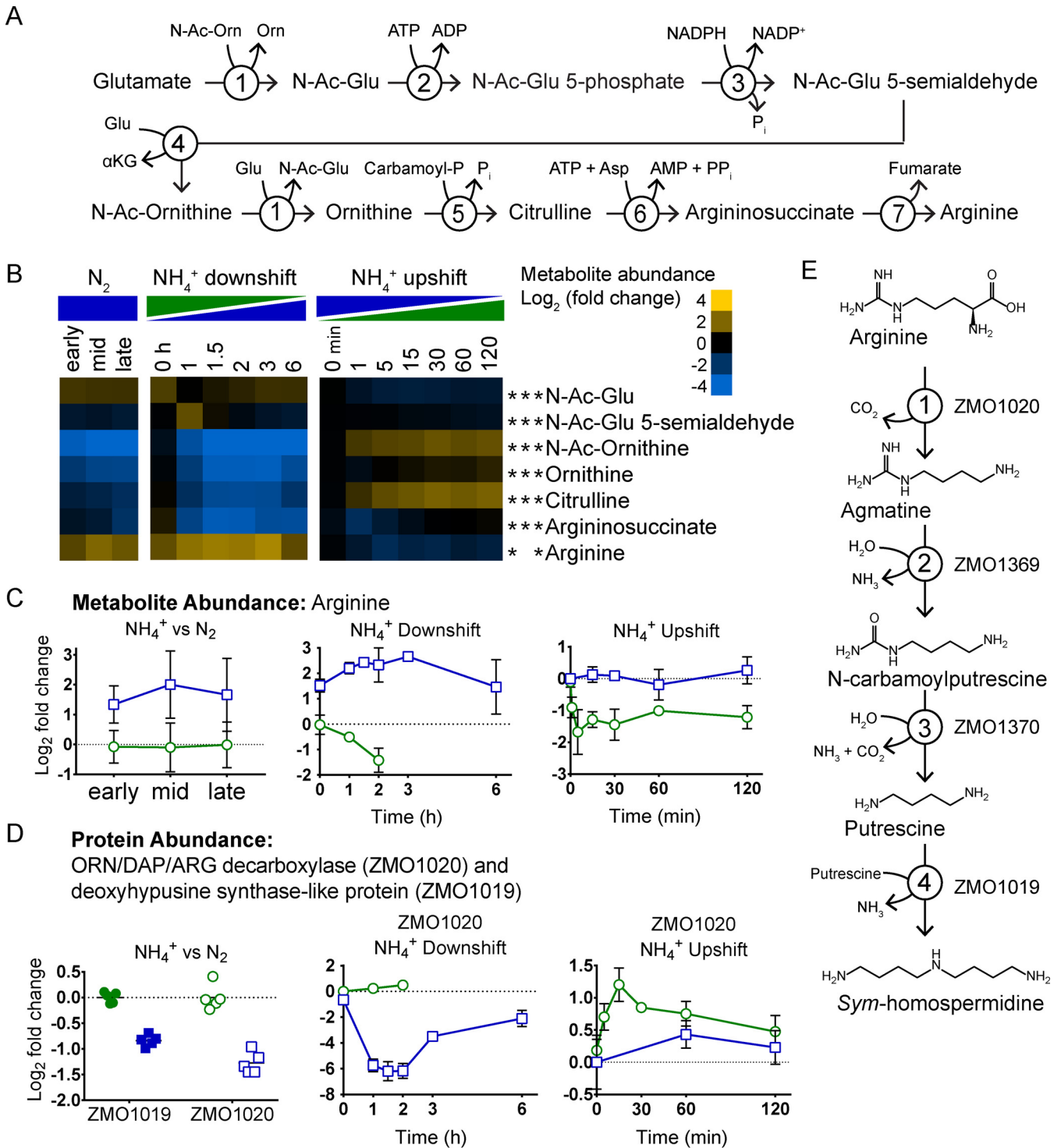
**Depletion of aromatic amino acids and shikimate pathway intermediates during N<sub>2</sub> fixation.** All three aromatic amino acids were significantly depleted under continuous N<sub>2</sub>-fixing conditions and during the dynamic shift to N<sub>2</sub>-fixing conditions. Intermediates of aromatic amino acid biosynthesis were also depleted under these conditions (Fig. 7). Of the seven intermediates of the shikimate pathway that we detected, all were found to be significantly depleted during continuous N<sub>2</sub> fixation (FC > 1.5, FDR < 0.05). Additionally, levels of 2-dehydro-3-deoxy-D-arabino-heptonate 7-phosphate (DAHP), shikimate 3-phosphate, and (to a lesser extent) phosphoenolpyruvate (PEP) all decreased significantly during the shift to N<sub>2</sub>-fixing conditions. Shikimate 3-phosphate showed dramatic changes, dropping to 24-fold below NH<sub>4</sub><sup>+</sup>-replete controls within the first hour. No changes were observed in levels of shikimate pathway intermediates during the NH<sub>4</sub><sup>+</sup> upshift.

**Arginine levels are elevated during N<sub>2</sub> fixation despite depletion of intermediates in arginine biosynthesis.** Of the 17 measured amino acids, arginine was the only amino acid that increased during NH<sub>4</sub><sup>+</sup> downshift and decreased during NH<sub>4</sub><sup>+</sup> upshift (Fig. 7 and 8C). Arginine was also the only amino acid with levels over 4-fold higher during continuous N<sub>2</sub> fixation than during NH<sub>4</sub><sup>+</sup>-replete conditions. These results were surprising given that biosynthesis of arginine requires more nitrogen than any other amino acid and may therefore be expected to be depleted under conditions of nitrogen limitation. However, examination of intracellular levels of intermediates in arginine biosynthesis provides a potential explanation for this apparent contradiction. Intracellular levels of all intermediates of arginine biosynthesis downstream of *N*-acetyl glutamate 5-semialdehyde (i.e., *N*-acetyl ornithine, ornithine, citrulline, and argininosuccinate) were depleted during both continuous N<sub>2</sub> fixation and the dynamic shift to N<sub>2</sub> fixation (Fig. 8A and B). During NH<sub>4</sub><sup>+</sup> upshift, intracellular concentrations of *N*-acetyl ornithine, ornithine, and citrulline all increased by over 1.5-fold (Fig. 8B). During continuous N<sub>2</sub> fixation, protein abundance of two enzymes in the arginine biosynthetic pathway (acetylglutamate kinase and argininosuccinate lyase) was significantly lower than in NH<sub>4</sub><sup>+</sup>-replete controls (see Fig. S3 in the supplemental material). However, no significant changes were observed in protein abundance of arginine biosynthetic enzymes during NH<sub>4</sub><sup>+</sup> downshift or upshift. Taken together, these data suggest that arginine biosynthesis does decrease during N<sub>2</sub> fixation. The fact that arginine still accumulates during N<sub>2</sub> fixation implies a decreased rate of arginine consumption.

#### **A potential pathway for *sym*-homospermidine biosynthesis from arginine.**

Examination of proteomics data identified a candidate enzyme potentially responsible for differential arginine consumption during N<sub>2</sub> fixation. Among the top 5 most differentially expressed proteins during the NH<sub>4</sub><sup>+</sup> downshift was a group IV decarboxylase, encoded by ZMO1020. Proteins of this family act as ornithine, diaminopimelate (DAP), or arginine decarboxylases (71). The ZMO1020 protein product decreased in abundance by 64-fold during the shift to N<sub>2</sub>-fixing conditions and remained severely depleted for 1 h (Fig. 8D). This severe depletion was somewhat transient, and after 6 h, protein levels were only 4-fold below the NH<sub>4</sub><sup>+</sup>-replete baseline. During NH<sub>4</sub><sup>+</sup> upshift, ZMO1020 protein levels increased by over 2-fold within 15 min of NH<sub>4</sub><sup>+</sup> addition (Fig. 8B). Under continuous N<sub>2</sub>-fixing conditions, the ZMO1020 protein was 2-fold less abundant than under NH<sub>4</sub><sup>+</sup>-replete conditions (Fig. 8D).

ZMO1020 is predicted to be in an operon with ZMO1019, which codes for a deoxyhypusine synthase-like protein (72). The ZMO1019 protein product was also depleted by around 2-fold during continuous N<sub>2</sub> fixation, although it did not change significantly during dynamic shifts in NH<sub>4</sub><sup>+</sup> availability (Fig. 8D). Another operon in *Z. mobilis* is predicted to encode agmatine deiminase (ZMO1369) and *N*-carbamoyl putrescine amidase (ZMO1370). It has been demonstrated that the major polyamine produced in *Z. mobilis* is *sym*-homospermidine (73). The enzymes encoded by ZMO1020, ZMO1369, ZMO1370, and ZMO1019 form a feasible biosynthetic route from arginine to *sym*-homospermidine (Fig. 8E) (74–77). In this case, the deoxyhypusine synthase-like



**FIG 8** (A) Arginine biosynthetic pathway. 1, *N*-acetyl-ornithine:glutamate *N*-acetyltransferase (*argJ*); 2, *N*-acetylglutamate 5-phosphotransferase (*argB*); 3, *N*-acetylglutamate 5-semialdehyde dehydrogenase (*argC*); 4, *N*-acetylornithine 5-aminotransferase (*argG*); 5, carbamoylphosphate:ornithine carbamoyltransferase (*argF*); 6, argininosuccinate synthetase (*argG*); 7, argininosuccinase (*argH*). (B) Relative intracellular metabolite abundance of intermediates in arginine biosynthesis. Log<sub>2</sub> fold change values are relative to the first time point in the control condition (not shown). Values are the averages of at least 3 biological replicates. Asterisks indicate statistical significance (FC ≥ 1.5, FDR ≤ 0.05) for NH<sub>4</sub><sup>+</sup> versus N<sub>2</sub>, NH<sub>4</sub><sup>+</sup> downshift, and NH<sub>4</sub><sup>+</sup> upshift conditions, respectively, from left to right. Metabolites were manually arranged by metabolic pathway order. (C) Relative intracellular metabolite abundance of arginine. (D) Relative protein abundance of ORN/DAP/ARG decarboxylase encoded by ZMO1020 and deoxyhypusine synthase-like protein encoded by ZMO1019. (C and D) Blue squares indicate N<sub>2</sub> fixation (or transition to N<sub>2</sub> fixation). Green circles indicate replete NH<sub>4</sub><sup>+</sup> (or NH<sub>4</sub><sup>+</sup> upshift). Log<sub>2</sub> fold change values are relative to first time point in the control condition. For NH<sub>4</sub><sup>+</sup> versus N<sub>2</sub> protein abundance, individual data points are shown (5 biological replicates per condition). For all other graphs, values are averages of at least 3 biological replicates for treatment condition and at least 2 biological replicates for control condition. Error bars show SD. (E) Hypothetical metabolic route from arginine to homospermidine via the enzymes encoded by ZMO1020, ZMO1019, ZMO1369, and ZMO1370. 1, arginine decarboxylase; 2, agmatine deiminase; 3, *N*-carbamoylputrescine amidase; 4, *sym*-homospermidine synthase.



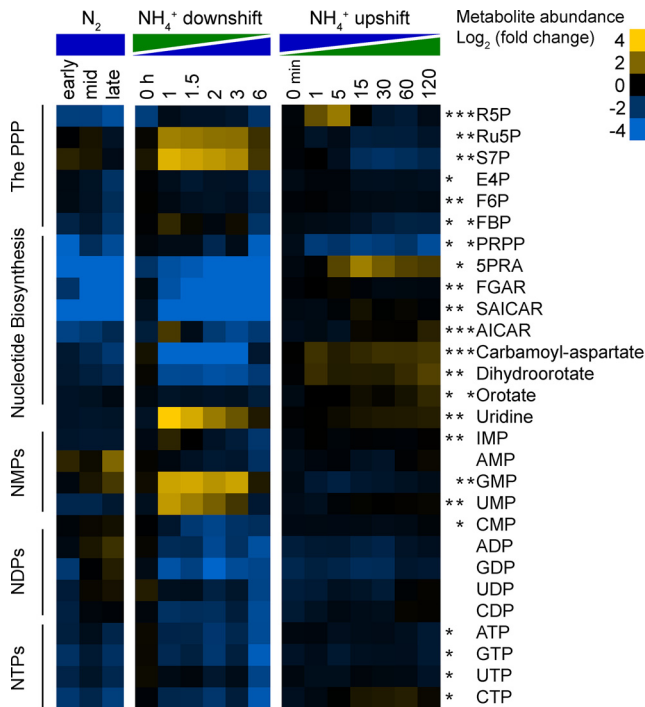
protein would function as a bacterial homospermidine synthase, combining two molecules of putrescine to generate *sym*-homospermidine. A similar pathway for *sym*-homospermidine production from arginine was identified in nitrogen-fixing cyanobacteria and was found to be required for robust diazotrophic growth (78). The negative correlation of arginine levels with ZMO1020 protein abundance, the organization of ZMO1020 and ZMO1019 genes within an operon, and the polyamine profile of *Z. mobilis* suggest that the protein encoded by ZMO1020 may function as an arginine decarboxylase, constituting the first step in *sym*-homospermidine biosynthesis in *Z. mobilis*. It is plausible that a shutdown of *sym*-homospermidine production during N<sub>2</sub> fixation caused the observed accumulation of intracellular arginine. Accumulation of arginine may have then triggered the depletion of arginine biosynthetic intermediates via feedback inhibition, as has been well documented in other bacteria (79). More research is needed to confirm the activity of the proposed biosynthetic pathway for *sym*-homospermidine in *Z. mobilis*.

While the precise physiological role of polyamines in bacteria remains an open area of discovery, polyamine production has been implicated in the response to a variety of environmental stressors, including high temperatures, oxidative stress, and acidic conditions (80–82). In our previous study of oxygen exposure in *Z. mobilis*, intracellular levels of arginine, acetyl-ornithine, and ornithine followed trends during the shift to aerobic conditions very similar to those during the shift to N<sub>2</sub>-fixing conditions (Fig. S4) (48). Additionally, protein abundance of the potential arginine decarboxylase encoded by ZMO1020 dropped sharply in response to oxygen exposure, as it did in response to NH<sub>4</sub><sup>+</sup> depletion (Fig. S4). These observations suggest that the hypothesized production of *sym*-homospermidine from arginine may be regulated in response to a variety of environmental stressors.

#### **Depletion of intermediates in nucleotide biosynthesis during N<sub>2</sub> fixation.**

Intermediates of *de novo* purine biosynthesis and *de novo* pyrimidine biosynthesis were depleted during both continuous N<sub>2</sub> fixation and the shift to N<sub>2</sub>-fixing conditions (Fig. 9). Of the two pathways, purine biosynthesis was more severely impacted, with purine biosynthetic intermediates such as 5-phosphoribosylamine (5PRA), phosphoribosyl-*N*-formylglycineamide (FGAR), and phosphoribosylaminoimidazole-succinocarboxamide (SAICAR) reaching over 180-fold below NH<sub>4</sub><sup>+</sup>-replete controls during the shift to N<sub>2</sub> fixation. The largest change observed in intermediates of pyrimidine biosynthesis was in carbamoyl aspartate, which dropped to 30-fold below baseline during the shift to N<sub>2</sub> fixation. During N<sub>2</sub> fixation, there was a general depletion of nucleotide triphosphates and nucleotide diphosphates but an accumulation of nucleotide monophosphates and nucleosides. During the NH<sub>4</sub><sup>+</sup> upshift, both 5PRA and carbamoyl aspartate increased significantly but nucleotide levels remained unchanged. The 5-fold increase in intracellular 5PRA was accompanied by a 5-fold decrease in phosphoribosyl diphosphate (PRPP) levels within 15 min of addition of NH<sub>4</sub><sup>+</sup>. This implies that amidophosphoribosyltransferase (PurF), which catalyzes the committed step in purine biosynthesis by incorporating an amino group from glutamine into PRPP to form 5PRA, is poised for rapid incorporation of nitrogen as soon as it becomes available (Fig. 9). This was consistent with rapid incorporation of <sup>15</sup>N into FGAR following <sup>15</sup>NH<sub>4</sub><sup>+</sup> addition (Fig. 6). We also observed dynamic changes in the PPP pathway following NH<sub>4</sub><sup>+</sup> upshift. In particular, ribose 5-phosphate (R5P) levels exhibited a sharp spike, reaching 5-fold above N<sub>2</sub>-fixing controls within 5 min of NH<sub>4</sub>Cl addition, only to drop back down to baseline by 15 min (Fig. S3). These trends highlight the tight regulation of PPP activity required to tune the supply of 5-carbon sugars for nucleotide biosynthesis during changes in nitrogen availability.

Despite the dramatic changes in intracellular metabolite levels of nucleotide biosynthetic intermediates, there were few significant changes in protein abundance of nucleotide biosynthetic enzymes during changes in NH<sub>4</sub><sup>+</sup> availability (Fig. S3). The only dynamic trend was a 1.7-fold decrease in PurF levels during the shift to N<sub>2</sub> fixation. The metabolic activity of nucleotide biosynthesis therefore appears to be regulated via the

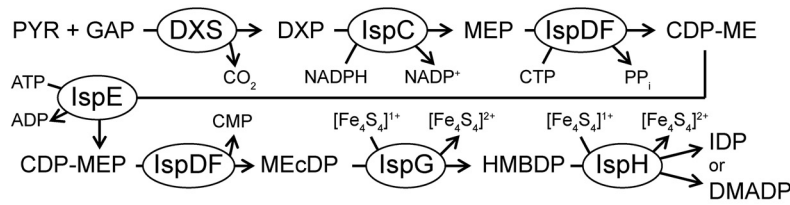
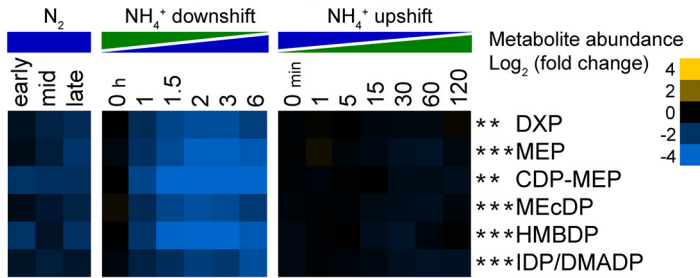
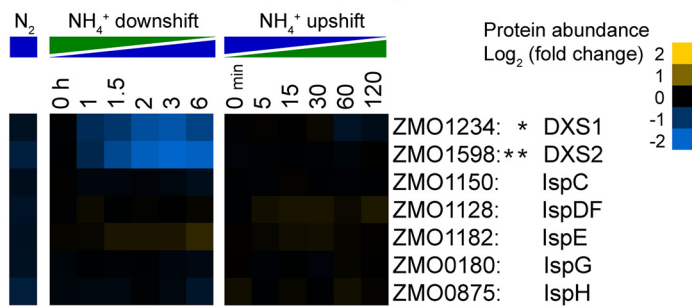


**FIG 9** Relative intracellular metabolite abundance of nucleic acids and intermediates in nucleic acid biosynthesis. Log<sub>2</sub> fold change values are relative to the first time point in the control condition (not shown). Values are the averages of at least 3 biological replicates. Asterisks indicate statistical significance ( $FC \geq 1.5$ ,  $FDR \leq 0.05$ ) for  $NH_4^+$  versus  $N_2$ ,  $NH_4^+$  downshift, and  $NH_4^+$  upshift conditions, respectively, from left to right. For example, intracellular levels of S7P changed significantly for  $NH_4^+$  downshift and  $NH_4^+$  upshift only and E4P changed significantly only for  $NH_4^+$  versus  $N_2$  conditions. Metabolites were manually arranged based on metabolic pathway and by number of phosphates for nucleotides. Abbreviations: R5P, ribose 5-phosphate; Ru5P, ribulose 5-phosphate; S7P, sedoheptulose 7-phosphate; E4P, erythrose 4-phosphate; F6P, fructose 6-phosphate; FBP, 1,6-fructose biphosphate; PRPP, phosphoribosyl diphosphate; 5PRA, 5-phosphoribosylamine; FGAR, phosphoribosyl-*N*-formylglycineamide; SAICAR, phosphoribosylaminoimidazole-succinocarboxamide; AICAR, 5-aminoimidazole-4-carboxamide ribonucleotide.

availability of nitrogen-containing metabolic precursors (e.g., amino acids) rather than the abundance of metabolic enzymes.

**Depletion of MEP pathway intermediates and decreased abundance of DXS during  $N_2$  fixation.** *Z. mobilis* exclusively utilizes the MEP pathway for the biosynthesis of isoprenoid precursors isopentenyl diphosphate (IDP) and dimethylallyl diphosphate (DMADP), which are required to produce biological compounds such as quinones and carotenoids (83). The MEP pathway starts with the condensation of pyruvate and glyceraldehyde 3-phosphate (GAP) to form 1-deoxy-D-xylulose 5-phosphate (DXP), catalyzed by DXS synthase (DXS). DXP is then converted to either IDP or DMADP via six enzymatic reactions carried out by IspC, IspD, IspE, IspF, IspG, and IspH (Fig. 10A). In *Z. mobilis*, there are two copies of the DXS enzyme (DXS1 and DXS2, encoded by ZMO1243 and ZMO1598, respectively) and IspD and IspF are fused and expressed as the single bifunctional enzyme IspDF.

Intracellular levels of all detected intermediates of the MEP pathway were lower during  $N_2$  fixation. Under continuous  $N_2$ -fixing conditions, MEP pathway intermediates were between 2-fold and 4-fold lower than  $NH_4^+$ -replete controls (Fig. 10B). During the dynamic shift to  $N_2$  fixation, an even more pronounced depletion was observed. All detected MEP pathway intermediates decreased by between 8-fold and 32-fold during the 6-h  $NH_4^+$  downshift time course (Fig. 10B). The intermediates 4-diphosphocytidyl-2-C-methyl-D-erythritol 2-phosphate (CDP-MEP) and 4-hydroxy-3-methyl-butenyl 1-diphosphate (HMBDP) displayed the largest decreases in abundance during both continuous  $N_2$  fixation and the shift to  $N_2$ -fixing conditions.  $NH_4^+$  upshift did not induce

**A Methylerythritol 4-phosphate (MEP) pathway****B Metabolite Abundance: MEP pathway intermediates****C Protein Abundance: MEP pathway enzymes**

**FIG 10** (A) Schematic of the MEP pathway. Abbreviations: PYR, pyruvate; GAP, glyceraldehyde 3-phosphate; DXP, 1-deoxy-D-xylulose 5-phosphate; MEP, 2-C-methylerythritol 4-phosphate; CDP-ME, 4-diphosphocytidyl-2-C-methyl-D-erythritol; CDP-MEP, 4-diphosphocytidyl-2-C-methyl-D-erythritol 2-phosphate; MEcDP, 2-C-methyl-D-erythritol 2,4-cyclodiphosphate; HMBDP, 4-hydroxy-3-methylbutenyl 1-diphosphate; IDP, isopentenyl diphosphate; DMADP, dimethylallyl diphosphate; DXS, DXP synthase. (B) Relative intracellular metabolite abundance of intermediates in the MEP pathway. Isomers IDP and DMADP were detected as a single combined signal. The intermediate CDP-ME was below our level of detection. (C) Relative protein abundance of MEP pathway enzymes. DXS1 and DXS2 share 98% amino acid identity. (B and C) Log<sub>2</sub> fold change values are relative to the first time point in the control condition (not shown). Values are the averages of at least 3 biological replicates. Yellow corresponds to increased metabolite abundance compared to the control, and blue indicates decreased metabolite abundance. Asterisks indicate statistical significance (FC ≥ 1.5, FDR ≤ 0.05) for NH<sub>4</sub><sup>+</sup> versus N<sub>2</sub>, NH<sub>4</sub><sup>+</sup> downshift, and NH<sub>4</sub><sup>+</sup> upshift conditions, respectively, from left to right. Metabolites and proteins were manually arranged by metabolic pathway order.

any increase in intracellular levels of MEP pathway intermediates, which all remained within 2-fold of the nitrogen-fixing control (Fig. 10B).

Of the seven enzymes of the MEP pathway, only the two DXS enzymes demonstrated significant changes in abundance in response to changes in NH<sub>4</sub><sup>+</sup> availability (Fig. 10C). All other MEP pathway enzymes remained within 1.5-fold of the control condition during all three nitrogen regimes. During continuous N<sub>2</sub> fixation, DXS2 protein levels were significantly lower than NH<sub>4</sub><sup>+</sup>-replete controls. During the NH<sub>4</sub><sup>+</sup> downshift experiment, both DXS1 and DXS2 decreased in abundance by over 3-fold within 3 h. However, following NH<sub>4</sub><sup>+</sup> upshift, neither DXS1 nor DXS2 changed in abundance during the 2-h time course.

Taken together, the trends in metabolite abundance of MEP pathway intermediates and protein abundance of MEP pathway enzymes suggest that MEP pathway activity is regulated during conditions of nitrogen limitation via abundance of the DXS enzyme.

This is an interesting observation considering that activity of the MEP pathway does not directly consume nitrogen. The fitness benefit of regulating the MEP pathway in response to nitrogen availability may be related to the pathway's consumption of ATP, CTP, or reduced cofactors. Additionally, decreased growth rates likely correspond to decreased demand for isoprenoid metabolites downstream of the MEP pathway. Others have reported experimental findings suggesting that the Clp protease complex may regulate MEP pathway activity in *Arabidopsis* plastids via degradation of DXS (84). More research is required to confirm targeted proteolytic degradation of DXS in *Z. mobilis* and to identify the mechanism of such degradation as well as the precise physiological cue, either nitrogen limitation itself or some secondary signal (for example depletion of NTP levels), that initiates the response.

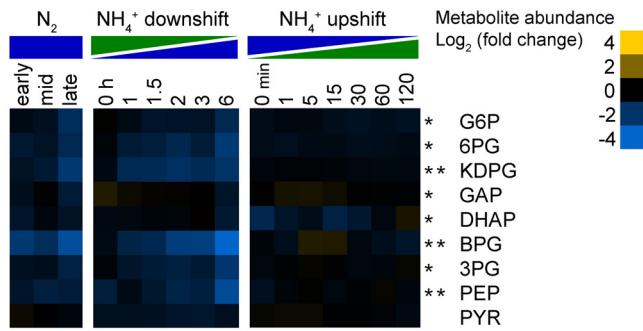
**Depletion of ED pathway intermediates and increased abundance of ADHI during N<sub>2</sub> fixation.** *Z. mobilis* utilizes the ED pathway exclusively for glucose catabolism (85, 86). Intracellular concentrations of all quantified ED glycolytic intermediates were significantly depleted (FC > 1.5, FDR < 0.05) during continuous N<sub>2</sub> fixation (Fig. 11A). Additionally, 2-keto-3-deoxy-6-phosphogluconate (KDPG), 1,3-bisphosphoglycerate (BPG), and phosphoenolpyruvate (PEP) levels decreased significantly during the shift to N<sub>2</sub>-fixing conditions (Fig. 11A). During the NH<sub>4</sub><sup>+</sup> upshift, no significant changes were observed for any intermediates of the ED pathway. Relative protein abundances of ED pathway enzymes were not significantly different during any of the three conditions of nitrogen availability, except for 6-phosphogluconolactonase (Pgl), which was 1.7-fold more abundant during continuous N<sub>2</sub> fixation (Fig. 11B).

During N<sub>2</sub> fixation, *Z. mobilis* exhibits increased specific rates of glucose consumption and ethanol production (17, 19, 20). However, the physiological factors that drive this response are not well understood. The *Z. mobilis* genome encodes two alcohol dehydrogenases, ADHI and ADHII. ADHI (encoded by *adhA*) is a zinc-dependent alcohol dehydrogenase, while ADHII (encoded by *adhB*) is iron dependent. Previous studies of purified ADHI and ADHII, and analysis of  $\Delta adhB$  strains, indicate that both ADHI and ADHII contribute to ethanol production (87–91). We found that protein levels of ADHI increased by 10-fold during the shift to N<sub>2</sub> fixation, placing it among the top 50 differentially abundant proteins observed in this study (Fig. 11C). No changes were observed in ADHI levels during continuous N<sub>2</sub> fixation or during the NH<sub>4</sub><sup>+</sup> upshift. ADHII did not significantly change in abundance during changes in NH<sub>4</sub><sup>+</sup> availability (Fig. 11C). The difference in metal cofactors used by the two ADH isozymes is especially relevant considering that expression of nitrogenase holoenzyme significantly increases the cellular demand for iron. Increasing expression of zinc-dependent ADHI rather than iron-dependent ADHII may be important for maintaining iron homeostasis. Increased ADHI expression may help explain the previously reported increase in specific ethanol production during N<sub>2</sub> fixation (17, 19, 20). However, the fact that no difference in ADHI abundance was detected during continuous N<sub>2</sub>-fixing conditions implies a possible difference in short-term and long-term mechanisms for increasing ethanol production.

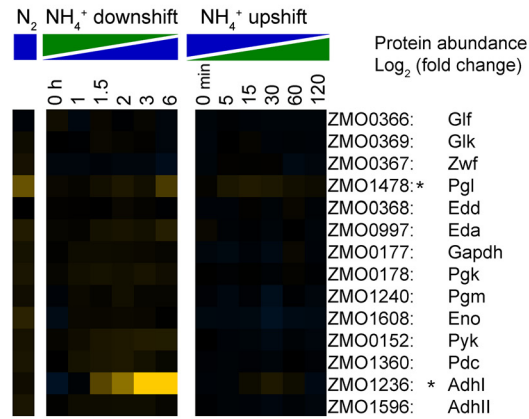
**Increased thermodynamic favorability of the ED pathway during N<sub>2</sub> fixation.** Thermodynamics constitutes a key determinant of flux and enzyme efficiency in metabolic networks. A pathway with a strong thermodynamic driving force (i.e., with an overall large negative change in Gibb's free energy or  $\Delta G$ ) will achieve a higher net flux given a fixed amount of enzyme activity than one closer to equilibrium (86, 92, 93). Within a pathway, steps closer to equilibrium will be the least enzyme efficient. A reaction's  $\Delta G$  is related to its reversibility or reverse-to-forward flux ratio ( $J^-/J^+$ ) by the equation  $\Delta G = RT \ln(J^-/J^+)$ , where  $R$  is the gas constant and  $T$  is the temperature in Kelvin. *In vivo* reaction reversibility, and thus thermodynamics, can be examined using isotope tracers.

To examine the impact of NH<sub>4</sub><sup>+</sup> availability on ED pathway thermodynamics, we grew cells on glucose positionally labeled with either <sup>13</sup>C or <sup>2</sup>H under continuous N<sub>2</sub>-fixing conditions and NH<sub>4</sub><sup>+</sup>-replete conditions. These experiments revealed that several reactions in the ED pathway were more reversible under NH<sub>4</sub><sup>+</sup>-replete conditions, implying increased thermodynamic favorability of the ED pathway during N<sub>2</sub> fixation

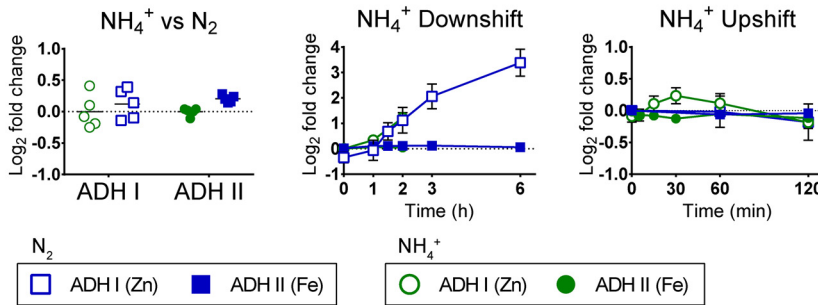
**A Metabolite Abundance: ED pathway intermediates**



**B Protein Abundance: ED pathway enzymes**



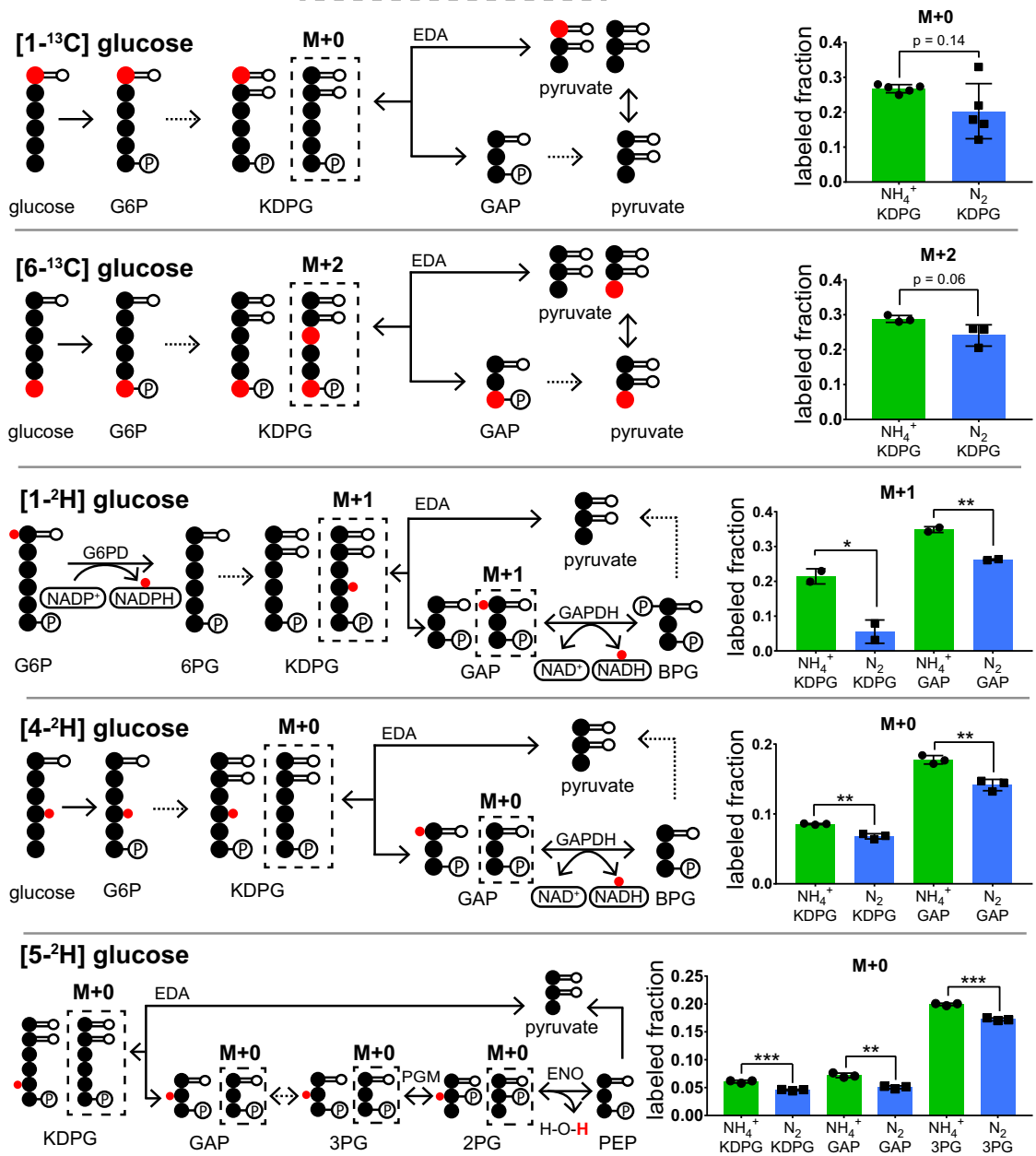
**C Protein Abundance: alcohol dehydrogenases**



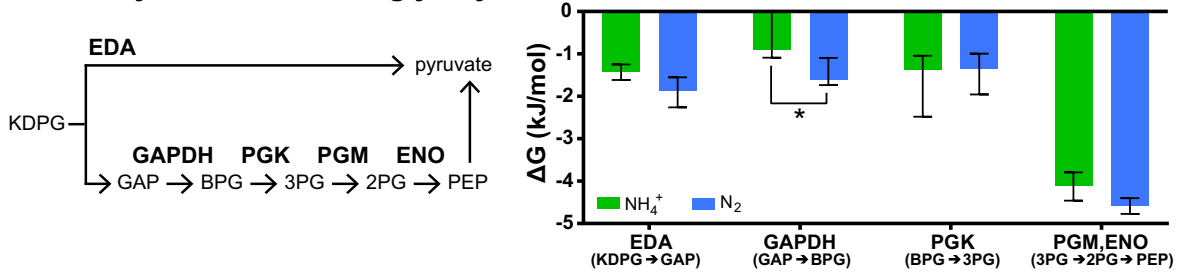
**FIG 11** (A) Relative intracellular metabolite abundance of intermediates in the Entner-Doudoroff glycolytic pathway. Abbreviations: G6P, glucose 6-phosphate; 6PG, 6-phosphogluconate; KDPG, 2-dehydro-3-deoxy-D-gluconate 6-phosphate; GAP, glyceraldehyde 3-phosphate; DHAP, dihydroxyacetone phosphate; BPG, 1,3-bisphosphoglycerate; 3PG, 3-phosphoglycerate; PEP, phosphoenolpyruvate; PYR, pyruvate. (B) Protein abundance of ED pathway enzymes and alcohol dehydrogenases. (A and B) Log<sub>2</sub> fold change values are relative to the first time point in the control condition (not shown). Values are the averages of at least 3 biological replicates. Asterisks indicate statistical significance (FC ≥ 1.5, FDR ≤ 0.05) for NH<sub>4</sub><sup>+</sup> versus N<sub>2</sub>, NH<sub>4</sub><sup>+</sup> downshift, and NH<sub>4</sub><sup>+</sup> upshift conditions, respectively, from left to right. Metabolites and proteins were manually arranged by metabolic pathway order. (C) Protein abundance of both Zn-dependent (ADHI, encoded by *adhA*) and Fe-dependent (ADHII, encoded by *adhB*) alcohol dehydrogenases. Blue squares indicate N<sub>2</sub> fixation (or transition to N<sub>2</sub> fixation). Green circles indicate replete NH<sub>4</sub><sup>+</sup> (or NH<sub>4</sub><sup>+</sup> upshift). Log<sub>2</sub> fold changes are relative to the first time point in the control condition. For NH<sub>4</sub><sup>+</sup> versus N<sub>2</sub> protein abundance, individual data points are shown (5 biological replicates per condition). For all other graphs, values are averages of at least 3 biological replicates for treatments and at least 2 biological replicates for the control condition. Error bars show SD. The only statistically significant change was in ADHI during NH<sub>4</sub><sup>+</sup> downshift.

(Fig. S5). In particular, labeling patterns of KDPG in cells fed either 100% [1-<sup>13</sup>C]glucose (98 to 99% isotopic purity) or 100% [6-<sup>13</sup>C]glucose (98 to 99% isotopic purity) indicated decreased reversibility of the KDPG aldolase reaction during N<sub>2</sub> fixation (Fig. 12A). Labeling patterns of GAP from cells fed 100% [1-<sup>2</sup>H]glucose (98% isotopic purity) or 100% [4-<sup>2</sup>H]glucose (98% isotopic purity) were consistent with decreased reversibility

**A Labeling Patterns**



**B Thermodynamics of lower glycolysis**



**FIG 12** (A, left) Schematics of isotopic labeling patterns expected from forward and reverse flux through the ED pathway. Black circles represent unlabeled (<sup>12</sup>C) carbon atoms. Large red circles represent <sup>13</sup>C-labeled carbon atoms. Small red circles represent <sup>2</sup>H hydrogen (deuterium) atoms (<sup>1</sup>H hydrogens not shown). Dashed boxes surround the labeled form of an intermediate that can be generated only by reverse flux through the ED pathway. Dashed arrows at a step indicate multiple enzymatic steps and not-shown intermediates. (A, right) (Continued on next page)



of GAP dehydrogenase during N<sub>2</sub> fixation (Fig. 12A). Labeling patterns of 3-phosphoglycerate (3PG) from cells fed 100% [5-<sup>2</sup>H]glucose (98% isotopic purity) were indicative of decreased reversibility of the two-step conversion of 3PG to PEP (Fig. 12A). Overall, the glycolytic reactions we observed were less reversible, and therefore more thermodynamically favorable, during N<sub>2</sub> fixation.

To provide a quantitative estimate of the effect of N<sub>2</sub> fixation on the thermodynamics of ED glycolysis, we fit glucose uptake rates, ethanol production rates, and labeling data from four <sup>13</sup>C and <sup>2</sup>H tracer experiments ([1-<sup>13</sup>C]glucose, [6-<sup>13</sup>C]glucose, [4-<sup>2</sup>H]glucose, and [5-<sup>2</sup>H]glucose) to a single flux map of ED glycolysis (Table S4). The equation  $\Delta G = RT \ln(J^-/J^+)$  was used to calculate reaction free energies for glycolytic reactions using forward-to-reverse flux ratios derived from metabolic flux analysis (MFA) (85, 94). For highly thermodynamically favorable reactions in upper ED glycolysis, i.e., glucose-6-phosphate 1-dehydrogenase (ZWF), 6-phosphogluconolactonase (PGL), and 6-phosphogluconate dehydratase (EDD), and the pyruvate kinase (PYK) reaction, forward-to-reverse flux ratios were not well resolved by MFA. Therefore, intracellular metabolite concentrations were used to provide tighter bounds on reaction free energies for these reactions, following the equation  $\Delta G = \Delta G^\circ + RT \ln(Q)$ , (where  $Q$  is the ratio of products to reactants) as previously described (85) (Table S4).

For highly favorable reactions (e.g., upper ED glycolysis), a small increase in  $\Delta G$  has a minimal impact on net forward flux, whereas for reactions that are closer to equilibrium (e.g., lower ED glycolysis), a modest increase in  $\Delta G$  can result in a substantial increase in net flux (92, 95). The MFA-derived free energies of lower ED pathway reactions are displayed in Fig. 12B and support the qualitative interpretation of the labeling data: glycolytic reactions tend to be more thermodynamically favorable during N<sub>2</sub> fixation than when NH<sub>4</sub><sup>+</sup> is supplied in the medium. The glyceraldehyde-3-phosphate dehydrogenase (GAPDH: GAP + NAD<sup>+</sup> + P<sub>i</sub> → BPG + NADH + H<sup>+</sup>) reaction in particular was significantly more thermodynamically favorable during N<sub>2</sub> fixation ( $P < 0.05$ ). The optimal solution  $\Delta G$  value of the GAPDH reaction was  $-1.617$  kJ/mol during N<sub>2</sub> fixation and  $-0.897$  kJ/mol when NH<sub>4</sub><sup>+</sup> was provided. The increased thermodynamic favorability of GAPDH may be due to increased consumption of reducing power by nitrogenase, thereby depleting one of the products (i.e., NADH) of the GAPDH reaction and driving the reaction forward. Other ED pathway reactions did not display significantly different free energies ( $P > 0.05$ ) but did trend toward greater thermodynamic favorability under N<sub>2</sub>-fixing conditions than under NH<sub>4</sub><sup>+</sup>-replete conditions (Fig. 12B; Table S4).

Increased thermodynamic favorability of glycolysis during N<sub>2</sub> fixation is a striking observation considering that the ED pathway in *Z. mobilis* is already highly thermodynamically favorable under NH<sub>4</sub><sup>+</sup>-replete conditions (85). High thermodynamic favorability of glycolysis has been proposed to contribute to high rates of glucose consumption (85, 86). A previous study found that in *E. coli*, thermodynamic favorability of the Embden-Meyerhof-Parnas (EMP) glycolytic pathway increased during an upshift in nitrogen or phosphorus availability, coinciding with an increased rate of glucose uptake (95). In *Z. mobilis*, increased thermodynamic favorability of the ED pathway may thus contribute to increased rates of glucose consumption and ethanol production.

### FIG 12 Legend (Continued)

Experimental labeling patterns of ED pathway intermediates extracted from *Z. mobilis* grown on isotopically labeled glucose. The y axis is the fraction of the metabolite pool that has a mass/labeling pattern consistent with reverse flux (indicated by graph title). M + 1 indicates the presence of one <sup>13</sup>C or one <sup>2</sup>H atom in the molecule; M + 0 indicates that all atoms are <sup>12</sup>C and <sup>1</sup>H. Green bars show average fractions of metabolite generated by reverse flux from cells grown with replete NH<sub>4</sub><sup>+</sup>, and blue bars show average fractions from cells grown under N<sub>2</sub>-fixing conditions. Individual samples are shown as black symbols. Error bars show SD.  $P$  values are from unpaired  $t$  tests comparing NH<sub>4</sub><sup>+</sup> with N<sub>2</sub> for each metabolite. See Fig. S5 in the supplemental material for the complete labeling patterns of all ED intermediates. (B, left) Schematic of reactions in the lower ED glycolytic pathway. (B, right) Change in free energy ( $\Delta G$ ) for glycolytic reactions during N<sub>2</sub> fixation (blue) or replete NH<sub>4</sub><sup>+</sup> availability (green).  $\Delta G$  values are calculated based on forward-to-reverse flux ratios derived from metabolic flux analysis (MFA) using the equation  $\Delta G = RT \ln(J^-/J^+)$ . Error bars represent 95% confidence intervals. Full results from the MFA model are reported in Table S4. Significance: \*,  $P < 0.05$ ; \*\*,  $P < 0.01$ ; \*\*\*,  $P < 0.001$ . Abbreviations: G6P, glucose 6-phosphate; 6PG, 6-phosphogluconate; KDPG, 2-dehydro-3-deoxy-D-gluconate 6-phosphate; GAP, glyceraldehyde 3-phosphate; BPG, 1,3-bisphosphoglycerate; 3PG, 3-phosphoglycerate; 2PG, 2-phosphoglycerate; PEP, phosphoenolpyruvate. Reactions: EDA, KDPG aldolase; GAPDH, GAP dehydrogenase; PGK, phosphoglycerate kinase; PGM, phosphoglycerate mutase; ENO, enolase (phosphopyruvate hydratase).

**Conclusions. (i) Regulation of nitrogenase activity in *Z. mobilis*.** The results of our metabolomics and proteomics analysis indicate that acute  $\text{NH}_4^+$  upshift induces decreased production of nitrogenase cofactors (e.g., FeS clusters, homocitrate) but not immediate, pronounced degradation of nitrogenase itself (Fig. 3 and 4). The decreased abundance of proteins involved in cofactor biogenesis (e.g., NifZ, NifB, NifU) and the decline in intracellular levels of homocitrate during  $\text{NH}_4^+$  upshift may play a role in downregulating nitrogenase activity. Proteolytic degradation of NifB, NifE, and NifN has been observed in *Azotobacter vinelandii* under  $\text{N}_2$ -fixing conditions and was found to be important for iron conservation (96). In *Z. mobilis*, rapid degradation of proteins involved in nitrogenase cofactor biogenesis in response to  $\text{NH}_4^+$  upshift may help to optimize iron utilization as soon as nitrogenase activity is no longer required.

Decreased biogenesis of nitrogenase cofactors may inhibit maturation or repair of new or damaged nitrogenase complexes but is not expected to inactivate holoenzyme. Indeed, tracer analysis using  $^{15}\text{NH}_4^+$  indicated that residual nitrogenase activity may persist for at least 2 h following  $\text{NH}_4^+$  upshift (Fig. 6). However, based on labeling patterns, only a small fraction of assimilated nitrogen is derived from non- $^{15}\text{NH}_4^+$  sources following  $\text{NH}_4^+$  upshift, suggesting that if residual nitrogenase activity persists, it is inhibited compared to its fully active state (Fig. 6). It is possible that posttranslational modification plays a role in reversibly inactivating nitrogenase during  $\text{NH}_4^+$  upshift, as has been demonstrated in other  $\text{N}_2$ -fixing bacteria (68–70). Differential phosphorylation of NifH and NifD during  $\text{N}_2$  fixation has been observed in *Z. mobilis* (60). However, *draT* and *draG*, the genes responsible for reversible inactivation of NifH via ADP-ribosylation in other organisms, have not been annotated in the *Z. mobilis* genome (30).

We previously reported a multi-omics analysis of oxygen exposure in *Z. mobilis* (48). Interestingly, unlike during the  $\text{NH}_4^+$  upshift, pronounced degradation of nitrogenase proteins did occur when cells were rapidly transferred from anaerobic to aerobic conditions during exponential growth. NifH, NifD, and NifK levels dropped to between 5-fold and 45-fold below anaerobic baseline within 2 h after oxygen exposure (48). The oxygen exposure time course was performed under  $\text{NH}_4^+$ -replete conditions, so the initial abundance of nitrogenase was lower than it was at the beginning of the  $\text{NH}_4^+$  upshift time course. However, the relative decrease in nitrogenase protein was much more pronounced during oxygen exposure than it was during  $\text{NH}_4^+$  upshift. *Z. mobilis* cultures immediately stop growing following a shift to aerobic conditions when  $\text{NH}_4^+$  is not supplied in the medium, suggesting that *Z. mobilis* lacks the ability to protect nitrogenase from oxidative damage (Fig. S6). A regulatory mechanism that stimulates high rates of nitrogenase protein degradation during oxygen exposure but delays complete degradation during  $\text{NH}_4^+$  upshift would therefore prevent detrimental accumulation of damaged nitrogenase while potentially allowing for rapid adaptation to fluctuating  $\text{NH}_4^+$  availability.

**(ii) Increased glycolytic activity may help meet increased energy demands associated with  $\text{N}_2$  fixation.** Regulation of carbon metabolism during changes in nitrogen availability is required to maintain the optimal ratio of carbon to nitrogen for biomass production. For most model microorganisms (e.g., *Escherichia coli*, *Bacillus subtilis*, *Saccharomyces cerevisiae*), decreased nitrogen availability results in a decreased rate of carbon uptake (97–99). However, for *Z. mobilis*, the opposite is true; nitrogen limitation results in increased specific glucose consumption despite decreased growth yield (17, 19, 100). In this study, we provide insight into the potential mechanisms driving this metabolic response, including decreased activity of biosynthetic pathways, increased protein abundance of ADHI, and increased thermodynamic favorability of the ED pathway during  $\text{N}_2$  fixation. The metabolic strategy for balancing carbon and nitrogen levels in *Z. mobilis* appears to leverage redirecting glucose toward ethanol production and away from biosynthetic reactions rather than decreasing glucose uptake. For *Z. mobilis*, glucose catabolism via the ED pathway is the only means of producing ATP, which is required to power  $\text{N}_2$  fixation by nitrogenase. Increased ED pathway activity may therefore be required to meet the high energy demands of  $\text{N}_2$  fixation. Additionally, the resulting increase in biomass-specific glucose consumption and

ethanol production may serve a competitive advantage in the glucose-rich ecological niches to which *Z. mobilis* is adapted (101).

A recent publication examined the effect of type 2 quorum sensing autoinducer (AI-2) on *Z. mobilis* physiology. Because *Z. mobilis* does not synthesize AI-2, its presence can be interpreted as an indication of the proliferation of competing microorganisms. The study found that AI-2 induced increased nitrogenase activity together with increased biomass-specific glucose consumption and ethanol production by *Z. mobilis* (20). Interestingly, this study also found that ED pathway genes were not consistently differentially transcribed in the presence of AI-2, but several carbohydrate transporters were. We did not observe any consistent increases in protein abundance of carbohydrate transporters during N<sub>2</sub> fixation in this study (Table S2). The glucose-facilitated diffusion protein (Glf) encoded directly upstream of the operon containing glucose-6-phosphate 1-dehydrogenase (*zwf*), phosphogluconate dehydratase (*edd*), and glucokinase (*glk*) genes was not differentially abundant at the protein level during any conditions of NH<sub>4</sub><sup>+</sup> availability (Fig. 11B) (102). Increased thermodynamic favorability of the ED pathway helps to explain the increase in biomass-specific glucose consumption rates during N<sub>2</sub> fixation despite no increases in the abundance of glucose transporters or glycolytic enzymes. Nitrogenase activity may directly contribute to the increased thermodynamic favorability of the ED pathway by consuming both energy (ATP) and reducing equivalents [NAD(P)H], two of the products of glycolysis. We found that intracellular levels of all NTPs were significantly lower under continuous N<sub>2</sub>-fixing conditions (Fig. 9). It is therefore possible that N<sub>2</sub>-fixing conditions result in increased specific rates of glucose consumption and ethanol production by reducing intracellular ATP and NAD(P)H concentrations, thereby driving increased flux through the ED pathway via thermodynamic control.

**(iii) Implications for biofuel production.** The results presented in this study provide valuable insight into the native regulation of metabolic pathways required for biofuel production in *Z. mobilis*. In particular, the MEP pathway is a metabolic engineering target for microbial production of isoprenoid bioproducts, including transport fuels, polymers, pharmaceuticals, fragrances, and flavor additives (103). Decreased concentrations of MEP pathway intermediates coincided with decreased abundance of DXS protein. The rate of DXS protein depletion was higher than the growth rate, implying active protein degradation rather than dilution by cell division. This suggests that DXS degradation natively inhibits MEP pathway activity in *Z. mobilis*, as has been proposed for *Arabidopsis* plastids (84). This finding has significant ramifications for metabolic engineering efforts to develop *Z. mobilis* as a platform organism for isoprenoid production. Metabolic engineering strategies often rely on transcription-based control of gene expression with the assumption that increased transcription will result in increased protein abundance. It will therefore be important to further investigate the mechanism of DXS protein degradation in order to avoid degradation-driven repression of MEP pathway activity in engineered strains.

The observation that the abundance of motility proteins decreased during N<sub>2</sub> fixation provides an interesting insight into native mechanisms for energy conservation in *Z. mobilis*. The impact of flagellar motility on the electrochemical gradient across the inner membrane is an important factor to consider for metabolic engineering. It is possible that deletion of motility genes may help conserve cellular energy, which could be directed to energy-intensive biofuel-producing pathways such as the MEP pathway.

Aside from isoprenoids, many bioproducts such as acetone, isobutanol, and butane-1,2-diol are derived from the products of glycolysis and compete with ethanol production for substrates. Understanding the native regulation of glycolysis and ethanol production is therefore critical in optimizing the production of these biofuels in a microbial system. Previous studies showed that specific ethanol production and specific glucose uptake both increased during N<sub>2</sub> fixation in *Z. mobilis* (17, 19, 20). In this study, we showed that the thermodynamic favorability of the ED glycolytic pathway increased during N<sub>2</sub> fixation and that the protein abundance of zinc-dependent alcohol

dehydrogenase ADHI increased during  $\text{NH}_4^+$  downshift. These findings help elucidate the underlying physiological mechanisms that drive changes in carbon utilization in *Z. mobilis* and will help inform metabolic engineering for increased conversion of sugars to bioproducts.

Finally, optimized performance of microbial biofuel producers requires not only maximal product generation but also robust and consistent growth despite the presence of diverse chemical inhibitors. Polyamines have long been appreciated to participate in the bacterial response to environmental stress, but the metabolic pathway for polyamine production in *Z. mobilis* is still unknown. Accumulation of arginine despite depletion of arginine biosynthetic intermediates suggests that polyamine production from arginine may be repressed during the transition to  $\text{N}_2$ -fixing conditions. Understanding the mechanism behind this metabolic response, and the physiological role of *sym*-homospermidine biosynthesis in stress tolerance, will therefore likely be informative in developing a robust biofuel-producing strain of *Z. mobilis*.

## MATERIALS AND METHODS

**Medium preparation.** To prepare the liquid minimal medium used in this study, a 10 $\times$  glucose solution (200 g/liter), 10 $\times$  base solution [10 g/liter  $\text{KH}_2\text{PO}_4$ , 10 g/liter  $\text{K}_2\text{HPO}_4$ , 5 g/liter NaCl, and either 10 g/liter  $(\text{NH}_4)_2\text{SO}_4$  or 2 g/liter  $\text{MgSO}_4$ ], and 1,000 $\times$  solutions of  $\text{MgSO}_4 \cdot 7 \text{H}_2\text{O}$  (200 g/liter),  $\text{Na}_2\text{MoO}_4 \cdot 2 \text{H}_2\text{O}$  (25 g/liter), and  $\text{CaCl}_2$  (10 g/liter) were prepared and autoclaved separately. One thousand-fold solutions of  $\text{FeSO}_4$  (2.5 g/liter) and calcium pantothenate (1 g/liter) were also prepared separately and filter sterilized using a 0.2- $\mu\text{m}$ -pore-size filter. Autoclaved deionized water was then aseptically combined with the separately sterilized solutions to produce 1 $\times$  concentrations of the added components. Finally, pH was measured to ensure that the medium was within the pH 6 to 6.5 range.

**Culture conditions.** *Zymomonas mobilis* subsp. *mobilis* strain ZM4 (ATCC 31821) was struck onto rich medium-glucose plates (20 g/liter glucose, 2 g/liter  $\text{KH}_2\text{PO}_4$ , 10 g/liter yeast extract, 18 g/liter agar) from a frozen 25% glycerol stock and incubated at 30°C in an anaerobic chamber for 3 to 6 days. For each biological replicate, a single colony was used to inoculate a flask of liquid minimal medium with replete ammonia [20 g/liter glucose, 1 g/liter  $\text{KH}_2\text{PO}_4$ , 1 g/liter  $\text{K}_2\text{HPO}_4$ , 0.5 g/liter NaCl, 1 g/liter  $(\text{NH}_4)_2\text{SO}_4$ , 0.2 g/liter  $\text{MgSO}_4 \cdot 7 \text{H}_2\text{O}$ , 25 mg/liter  $\text{Na}_2\text{MoO}_4 \cdot 2 \text{H}_2\text{O}$ , 2.5 mg/liter  $\text{FeSO}_4 \cdot 7 \text{H}_2\text{O}$ , 0.01 g/liter  $\text{CaCl}_2 \cdot 2 \text{H}_2\text{O}$ , 1 mg/liter calcium pantothenate]. After 14 to 16 h of growth, a small volume (10  $\mu\text{l}$  to 1 ml) of this culture was used to inoculate subsequent cultures which contained either 15 mM  $\text{NH}_4^+$  or no  $\text{NH}_4^+$ . In the case of no- $\text{NH}_4^+$  minimal medium, the 1 g/liter  $(\text{NH}_4)_2\text{SO}_4$  was replaced with 0.2 g/liter  $\text{MgSO}_4$  to achieve similar molarity. All cultures were grown in foil-covered Erlenmeyer flasks with an approximately 1:5 ratio of liquid volume-to-flask capacity. The total liquid volume ranged from 25 ml (in 125-ml flasks) to 100 ml (in 500-ml flasks). Cultures were stirred with a magnetic stir bar set to 120 rpm. All medium was kept anaerobic for at least 16 h prior to inoculation. The atmosphere in the anaerobic chamber was composed of 2 to 4%  $\text{H}_2$ , 5%  $\text{CO}_2$ , and the remaining percentage  $\text{N}_2$ . Oxygen levels were kept below 100 ppm.

**Comparison of  $\text{N}_2$  and  $\text{NH}_4^+$ .** To compare continuous  $\text{N}_2$  fixation to  $\text{NH}_4^+$ -replete conditions, each of three separate  $\text{NH}_4^+$ -replete starting cultures were used to inoculate minimal medium with 15 mM  $\text{NH}_4^+$  (replete) and minimal medium with no  $\text{NH}_4^+$  ( $\text{N}_2$ -fixing conditions), resulting in three biological replicates per condition. These cultures were grown anaerobically for up to 16 h. Before reaching stationary phase, cultures were used to inoculate fresh medium, maintaining the same  $\text{NH}_4^+$  availability. Again, before reaching stationary phase, the second set of cultures was used to inoculate experimental flasks with a starting optical density at 600 nm ( $\text{OD}_{600}$ ) of approximately 0.05. This passaging was performed both to ensure continuous  $\text{NH}_4^+$  availability and to dilute any nutrients provided by the rich medium plate. The result was that experimental cultures for the  $\text{N}_2$ -fixing condition were inoculated with cells that had been growing under  $\text{N}_2$ -fixing conditions for at least 6 doublings. Following inoculation of experimental cultures, extractions were performed for intracellular metabolite analysis during early, mid-, and late exponential phase ( $\text{OD}_{600}$  of 0.3, 0.5, and 0.7, respectively) for both  $\text{NH}_4^+$ -replete and  $\text{N}_2$ -fixing cultures. For proteomics, a separate experiment was conducted with the same culture inoculation protocol except that there were five replicates instead of three. Extractions for proteomic analysis were performed at mid-exponential phase ( $\text{OD}_{600}$  of 0.5) only.

**$\text{NH}_4^+$  downshift.** To examine the transition to  $\text{N}_2$ -fixing conditions, two rounds of passaging were performed as described for the  $\text{N}_2$  versus  $\text{NH}_4^+$  experiment, except that all passaging was done in medium containing 15 mM  $\text{NH}_4^+$ . Flasks containing medium with either no  $\text{NH}_4^+$  or 15 mM  $\text{NH}_4^+$  were then inoculated using the cultures that had been passaged in replete  $\text{NH}_4^+$ . The inoculation volume was such that  $\text{NH}_4^+$  carryover was sufficient to sustain a 2-h doubling time for 6 h after inoculation into medium containing no additional  $\text{NH}_4^+$ . Based on inoculation volume, the carryover from inoculation resulted in an initial  $\text{NH}_4^+$  concentration of less than 2 mM. During the  $\text{NH}_4^+$  downshift experiment, metabolomics and proteomics analyses were performed at the same time, sampling from the same cultures. The  $\text{NH}_4^+$  downshift condition had biological triplicates and the  $\text{NH}_4^+$ -replete controls had biological duplicates. The first extraction for metabolomics and proteomics analysis was performed for both conditions 5.5 h after inoculation ( $\text{OD}_{600}$  of 0.35), when growth was still exponential for both conditions. For the  $\text{NH}_4^+$  downshift condition, subsequent samples were taken at 1, 1.5, 2, 3, and 6 h after the first sample. For the  $\text{NH}_4^+$  repletion condition, samples were taken at 1 and 2 h after the first sample.

**NH<sub>4</sub><sup>+</sup> upshift.** For the NH<sub>4</sub><sup>+</sup> upshift experiment, two rounds of passaging were performed as described for the N<sub>2</sub> versus NH<sub>4</sub><sup>+</sup> experiment, except that all passaging was done in medium containing no NH<sub>4</sub><sup>+</sup>. Flasks containing medium with no NH<sub>4</sub><sup>+</sup> were then inoculated using the cultures that had been passaged under N<sub>2</sub>-fixing conditions. Approximately 6 h after inoculation (OD<sub>600</sub> of approximately 0.35), the first extraction for metabolomics and proteomics analysis was performed for all cultures. Immediately following this extraction, 1.5 ml of a 1 M NH<sub>4</sub>Cl solution (15 mM final concentration) was added to three experimental cultures, leaving two cultures as N<sub>2</sub>-fixing controls. Subsequently, extractions were taken at 5, 15, 30, 60, and 120 min after addition of NH<sub>4</sub>Cl for the NH<sub>4</sub><sup>+</sup> upshift condition. For the N<sub>2</sub>-fixing controls, extractions were taken at 60 and 120 min after the first extraction. This experiment was also performed using <sup>15</sup>NH<sub>4</sub>Cl, without proteomics sampling. For the <sup>15</sup>N-labeled iteration, metabolomics time point samples were collected at 1, 5, 15, 30, 60, and 120 min after addition of NH<sub>4</sub><sup>+</sup> for the NH<sub>4</sub><sup>+</sup> upshift condition and at 15, 30, 60, and 120 min after the first extraction for the N<sub>2</sub>-fixing controls. An additional replicate was also included for the control condition in this iteration, resulting in biological triplicates for both conditions.

**Stable isotope labeling.** [1-<sup>13</sup>C]D-glucose (CLM-420-PK) (98 to 99% isotopic purity), [6-<sup>13</sup>C]D-glucose (CLM-481-PK) (98 to 99% isotopic purity), [1-<sup>2</sup>H]D-glucose (DLM-1150-PK) (98% isotopic purity), [4-<sup>2</sup>H]D-glucose (DLM-9294-PK) (98% isotopic purity), [5-<sup>2</sup>H]D-glucose (DLM-6754-PK) (98% isotopic purity), and <sup>15</sup>NH<sub>4</sub>Cl (NLM-467-PK) (98 to 99% isotopic purity) were purchased from Cambridge Isotope Laboratories, Inc. For all labeling data in this study, masses were adjusted to account for the natural abundance of <sup>15</sup>N, <sup>13</sup>C, or <sup>2</sup>H using ElemCor (104). For thermodynamics analysis, 10× glucose stock solutions were prepared using autoclaved deionized water and sterilized by passage through a 0.2-μm filter. Both NH<sub>4</sub><sup>+</sup> and N<sub>2</sub> conditions were grown with 15 g/liter glucose to reduce costs. Growth rates were the same as in 20 g/liter glucose. Cultures were passaged as described for the N<sub>2</sub> versus NH<sub>4</sub><sup>+</sup> experiment, except that the final passage before inoculation into experimental flasks was performed in 4-ml volumes in culture tubes containing medium with labeled glucose matching the labeled glucose present in experimental flasks. This was done to minimize unlabeled carryover from inoculation. Metabolite extractions were performed from experimental flasks 5 to 12 h after inoculation, when cultures reached an OD<sub>600</sub> of 0.35.

**Metabolic flux analysis and goodness of fit.** A *Z. mobilis* metabolic model was adapted from a report by Jacobson et al. in 2019 and simplified to include only reactions for glucose uptake, ED glycolysis, and ethanol production (85). Reversible reactions were modeled as separate forward and backward reactions. Within the model, cellular H<sup>+</sup> and CO<sub>2</sub> were allowed to freely exchange with naturally labeled equivalents. Metabolic flux analysis was performed using the INCA software suite (105), which is implemented in MATLAB and uses the elementary metabolite unit (EMU) framework to simulate isotopic distributions (106). We combined labeling data from our <sup>13</sup>C and <sup>2</sup>H tracer experiments ([1-<sup>13</sup>C]glucose, [6-<sup>13</sup>C]glucose, [4-<sup>2</sup>H]glucose, and [5-<sup>2</sup>H]glucose) with glucose uptake and ethanol excretion rates provided by Jake McKinlay (17) to create a single, statistically acceptable flux map using the COMPLETE-MFA technique (107). Glucose tracer inputs were defined by label type (<sup>13</sup>C or <sup>2</sup>H) and position, but the proportion of unlabeled glucose was allowed to vary by modeling glucose uptake as two glucose inputs, one labeled and one unlabeled, whose relative contribution was controlled by the flux fit optimization process. Final model solutions estimate the unlabeled fraction of glucose at approximately 1%, consistent with nominal tracer purity. Metabolite mass isotopomer distribution (MID) precision was estimated by combining the variance of each measurement across biological replicates and the maximum error observed from naturally labeled metabolites compared to the theoretical MID calculated from natural isotope abundances with a minimum allowable error of 0.3% for each MID, as previously described (85). The combined <sup>2</sup>H and <sup>13</sup>C best-fit flux solutions are contained in Table S4 in the supplemental material. Labeling data from <sup>13</sup>C and <sup>2</sup>H tracer experiments were used in INCA without prior correction for naturally abundant heavy isotopes.

Intracellular fluxes were estimated by solving a nonlinear least-squares regression problem that minimizes the variance-weighted sum of square residuals (SSR) between simulated and measured isotopic distributions of intracellular and extracellular metabolites. Because the solver does not guarantee a global SSR optimum, we used a random multistart approach until SSR improvement ceased. Using the optimal solution, we calculated 95% confidence intervals for all estimated fluxes by individually varying each flux and testing the sensitivity of the optimal SSR to changes in that flux. Upper and lower bounds were assigned by varying each flux until the SSR was perturbed beyond a critical point corresponding to a chi-square distribution with a single degree of freedom.

A  $\chi^2$  test was used to determine whether estimated fluxes adequately describe the measured labeling data. A correct model and data set have an optimized SSR that falls within a  $\chi^2$  distribution with degrees of freedom equal to the fitted measurements (i.e., non-zero MIDs and measured fluxes, such as uptake and excretion rates) minus the number of independent parameters (i.e., all fluxes estimated by the analysis). We set the critical threshold of our  $\chi^2$  test at 0.05 (95% confidence) and required that optimized SSRs fell within this distribution for acceptance. We attempted to fit labeling data from *Z. mobilis* grown under NH<sub>4</sub><sup>+</sup>-replete conditions together with data from N<sub>2</sub>-fixing conditions to a single flux map and were unable to find a statistically acceptable fit, suggesting that these two conditions are distinct metabolic states for *Z. mobilis*.

**Metabolite extraction.** At the time of extraction, 5 to 10 ml of liquid culture was extracted using a serological pipette. The culture was then rapidly filtered through a 0.45-μm nylon filter (Millipore catalog no. HNWP04700) using a vacuum flask fitted with a sintered glass funnel, separating cells from the growth medium. Immediately after the medium passed through the filter, the cells captured on the filter were plunged into cold extraction solvent, simultaneously quenching metabolism, lysing cells, and dissolving intracellular metabolites. This was done by placing the filter facedown in a small (5.5-cm-



diameter) plastic petri dish containing 1.5 ml extraction solvent (40:40:20 methanol-acetonitrile-water; all high-performance liquid chromatography [HPLC] grade). The dish containing extraction solvent was kept on dry ice or an aluminum block that had been stored at  $-80^{\circ}\text{C}$ . The entire process of extraction was done in 30 s or less. The filter was then rinsed in the extraction solvent within the dish using a pipette to dislodge remaining cell debris and metabolites. The 1.5 ml of extract was then transferred to a microcentrifuge tube and centrifuged at  $16,000 \times g$  for 3 min to remove debris. The supernatant was stored at  $-80^{\circ}\text{C}$  until analysis by LC-MS. For analysis, 300 to 200  $\mu\text{l}$  of extract was dried down under  $\text{N}_2$  gas. Samples were concentrated three times by resuspension in one-third the dry-down volume of solvent A (see "Metabolomics LC-MS analysis"), vortexed for 10 s, and centrifuged at  $16,000 \times g$  for 3 min to remove any remaining cell debris. Fifty microliters of the supernatant was then transferred to an HPLC vial for LC-MS analysis.

**Metabolomics LC-MS analysis.** Metabolomics analysis by LC-MS was performed using a Vanquish ultra-high-performance LC (UHPLC) system (Thermo Scientific) coupled to a hybrid quadrupole orbitrap mass spectrometer (Q Exactive, Thermo Scientific), as previously described (23, 48, 108). The chromatography was done using a reverse-phase  $\text{C}_{18}$  column (1.7- $\mu\text{m}$  particle size, 2.1- by 100-mm column; Acquity UPLC BEH). Solvent A was 97%  $\text{H}_2\text{O}$  and 3% methanol with 10 mM tributylamine (TBA) and  $\sim 10$  mM acetic acid for a pH of 8.2. Solvent B was 100% methanol. The total run time was 25 min. The flow rate was held constant at 0.2 ml/min. The chromatography gradient was as follows: 5% solvent B for 2.5 min, linear increase to 95% B over 14.5 min, maintenance of 95% B for 2.5 min, linear decrease back to 5% B over 0.5 min, maintenance of 5% B for 5 min. Eluent from the column was analyzed by mass spectrometry from the start of the run until 19 min, at which time flow was directed to waste for the remainder of the run. Compounds separated by HPLC were ionized by electrospray ionization (negative polarity) and analyzed by full MS-selected ion monitoring (MS-SIM) with a scanning range of 70 to 1,000  $m/z$ , an automatic gain control (AGC) target value of  $1 \times 10^6$ , maximum injection time (IT) of 40 ms, and resolution of 70,000.

**Metabolomics computational analysis.** LC-MS raw files were converted to mzXML format and visualized using MAVEN (109). Peaks were chosen by comparison with retention times obtained using analytical standards. To account for slight signal variation from injection to injection, samples were either run twice (technical duplicate) and averaged or mixed 1:1 with a universally  $^{13}\text{C}$ -labeled intracellular metabolite sample harvested from *E. coli* grown in  $[\text{U}-^{13}\text{C}]_6$ -glucose and normalized by  $\text{U}-^{13}\text{C}$  signal, as previously described (48). For each metabolite, signal intensity was divided by  $\text{OD}_{600}$  to account for variation in culture density between samples. These values were then divided by the average of the three replicates in the control sample to generate fold change values. For  $\text{N}_2$  versus  $\text{NH}_4^+$ , the control sample was  $\text{NH}_4^+$ -replete conditions at early exponential phase. For  $\text{NH}_4^+$  downshift, the control sample was  $\text{NH}_4^+$ -replete conditions at time zero. For  $\text{NH}_4^+$  upshift, the control sample was  $\text{N}_2$ -fixing conditions at time zero. The  $\log_2$  of the fold change values was then averaged to obtain the data displayed in this study.

**Protein extraction and preparation.** At the time of extraction, 4 ml of culture was collected and cells were pelleted by centrifugation for 3 min at  $16,000 \times g$ . Supernatant was discarded, and pellets were frozen and stored at  $-80^{\circ}\text{C}$  until further analysis. Samples were prepared for LC-tandem MS (LC-MS/MS) analysis by thawing and then lysing cells in 900  $\mu\text{l}$  of methanol, resulting in a final concentration of over 90% methanol. Samples were kept cold at  $4^{\circ}\text{C}$  for 30 min and then centrifuged for 20 min at  $15,000 \times g$ . Supernatant was removed, and protein extract was air dried at room temperature. The protein pellet was resuspended in 50  $\mu\text{l}$  8 M urea, 100 mM Tris (pH 8.0)–10 mM TCEP [Tris(2-carboxyethyl)phosphine hydrochloride], and 40 mM chloroacetamide to denature, reduce, and alkylate proteins. Sonication for 10 min ensured that all protein was in solution. The protein concentration was determined with NanoDrop using the A280 method. The protein resuspension was diluted to 1.5 M urea in 100 mM Tris (pH 8.0) and sonicated for 10 min. Trypsin was added at an estimated 50:1 ratio, and samples were incubated overnight (12 h) at ambient temperature. After incubation with digestion enzyme, each sample was prepared for desalting using a 96-well Strata polymeric reversed-phase 10-mg SPE (styrene divinylbenzene) cartridge. Preparation included priming the cartridge wells with 1 ml of ACN (acetonitrile), followed by 1 ml of 0.1% trifluoroacetic acid (TFA). Each sample was acidified with TFA to a final pH of 2.0 or less and then centrifuged for 15 min at  $2,000 \times g$  to remove all nonprotein material. Acidified sample was then loaded onto the cartridge, washed with 1 ml of 0.1% TFA, and then eluted with 600  $\mu\text{l}$  of 80% ACN–0.1% TFA into a clean 96-well plate to be dried. Samples were resuspended in 0.2% formic acid, and peptide mass was assayed with NanoDrop A280 for a final concentration close to 1  $\mu\text{g}/\mu\text{l}$ .

**Proteomics LC-MS/MS analysis.** Proteomics analysis was performed as previously described (22, 25, 26). For each analysis, 1  $\mu\text{g}$  of peptides was loaded onto a 75- $\mu\text{m}$ -inside-diameter (i.d.), 30-cm-long capillary with an embedded electrospray emitter and packed in a 1.7- $\mu\text{m}$ -particle-size  $\text{C}_{18}$  BEH column (stationary phase). The mobile phases used were as follows: phase A, 0.2% formic acid; phase B, 0.2% formic acid–70% acetonitrile. The peptides were eluted with a gradient of acetonitrile increasing from 0% to 50% B over 74 min followed by a 1-min increase to 100% B, 5 min sustained at 100% B, and a final 10 min of equilibration in 100% A. The eluting peptides were analyzed with an Orbitrap Eclipse (Thermo Fischer Scientific) mass spectrometer. Survey scans were performed at a resolution of 240,000 with an isolation analysis at  $m/z$  300 to 1,350 and 250% normalized automatic gain control (AGC) target. Data-dependent top-speed (1-s) MS/MS sampling of peptide precursors was enabled with dynamic exclusion set to 10 s on precursors with charge states 2 to 5. Data-dependent MS/MS sampling was performed with 0.5-Da quadrupole isolation, with fragmentation by higher-energy collisional dissociation (HCD) with a normal collisional energy (NCE) value of 300%. The mass analysis was performed in the ion trap using the "turbo" scan speed for a mass range of 150 to 1,350  $m/z$  with a maximum inject time of 14 ms, and the normalized AGC target set to 300%.



**Proteomics computational analysis.** Raw files were analyzed using MaxQuant 1.5.8.3 (110). Spectra were searched using the Andromeda search engine against a decoy target list. Label-free quantitation and match between runs were toggled on, MS/MS tolerance was set to 0.4 Da, and the number of measurements for each protein was set to 1. Default values were used for all other analysis parameters. The peptides were grouped into subsumable protein groups and filtered to reach 1% FDR, based on the target decoy approach. The fasta database “Zm4.CDS.AA.fasta” was used to generate the protein list utilizing the ZM4 tag for protein names. Using RStudio, the label-free quantitation (LFQ) values and protein intensities in each sample were log<sub>2</sub> transformed and filtered to contain proteins that fulfill a >50% cutoff of measurements across the samples. The average and standard deviation were calculated across the replicates for each protein, and fold changes are relative to control time zero for each experiment.

**Statistical analysis.** Statistical analysis for metabolomics and proteomics data sets was performed in R. For metabolomics, raw signal intensity was normalized by OD<sub>600</sub> and then log<sub>2</sub> transformed before statistical analysis. For proteomics, the log<sub>2</sub> of LFQ values was used. For both metabolomics and proteomics time courses, a repeated-measures analysis of variance (ANOVA) test was performed for each metabolite or protein, comparing time points within the treatment group. This tests the null hypothesis that the mean value for metabolite or protein abundance was not different at any time during the time course. The *P* values from the repeated-measures ANOVA tests were then adjusted for multiple hypothesis testing using the Benjamini-Hochberg method to control for false discovery rate (FDR) (111). In this case, an FDR-adjusted *P* value below 0.05 indicates that less than 5% of proteins or metabolites identified as changing during changes in NH<sub>4</sub><sup>+</sup> availability are false positives. For metabolomics during continuous N<sub>2</sub>-fixing conditions compared to continuous NH<sub>4</sub><sup>+</sup>-replete conditions, a two-way repeated-measures ANOVA test was performed to test the null hypothesis that the average metabolite abundance was not different between N<sub>2</sub>-fixing and NH<sub>4</sub><sup>+</sup>-replete conditions, independent of growth stage. The *P* values from this test were adjusted for multiple hypothesis testing using the Benjamini-Hochberg method. For proteomics during continuous NH<sub>4</sub><sup>+</sup> availability, an unpaired *t* test was performed to test the null hypothesis that the average protein abundance was not different between N<sub>2</sub>-fixing and NH<sub>4</sub><sup>+</sup>-replete conditions. The *P* values from this test were adjusted for multiple hypothesis testing using the Benjamini-Hochberg method. For <sup>15</sup>N isotope tracers, a repeated-measures ANOVA was performed to test the null hypothesis that the average fraction of M + 2 glutamine was not different at any time point between 15 min and 2 h. For thermodynamic analysis using isotopic labeling, statistical analysis was performed in GraphPad Prism. For this data set, an unpaired *t* test was performed for each metabolite shown in Fig. 12, testing the null hypothesis that the average fraction of reverse-flux-associated labeled form was not different between N<sub>2</sub>-fixing and NH<sub>4</sub><sup>+</sup>-replete conditions.

**Data availability.** The mass spectrometry proteomics data have been deposited in the ProteomeXchange Consortium via the PRIDE (112) partner repository with the data set identifier PXD028526. Metabolomics data have been deposited in the Open Science Framework (<https://osf.io>) (113) under the project “N<sub>2</sub> fixation in *Zymomonas mobilis*” at <https://doi.org/10.17605/OSF.IO/GJYVW>.

## SUPPLEMENTAL MATERIAL

Supplemental material is available online only.

**FIG S1**, EPS file, 1.2 MB.

**FIG S2**, EPS file, 1 MB.

**FIG S3**, EPS file, 1.6 MB.

**FIG S4**, EPS file, 1.2 MB.

**FIG S5**, EPS file, 1.1 MB.

**FIG S6**, EPS file, 0.6 MB.

**TABLE S1**, XLSX file, 0.1 MB.

**TABLE S2**, XLSX file, 0.6 MB.

**TABLE S3**, XLSX file, 0.02 MB.

**TABLE S4**, XLSX file, 0.02 MB.

## ACKNOWLEDGMENTS

This material is based upon work supported by the Great Lakes Bioenergy Research Center, U.S. Department of Energy, Office of Science, Office of Biological and Environmental Research under award numbers DE-SC0018409 and DE-FC02-07ER64494 and the Early Career Research Program under award number DE-SC0018998.

## REFERENCES

- Swings J, De Ley J. 1977. The biology of *Zymomonas*. *Bacteriol Rev* 41: 1–46. <https://doi.org/10.1128/br.41.1.1-46.1977>.
- He M, Wu B, Qin H, Ruan Z, Tan F, Wang J, Shui Z, Dai L, Zhu Q, Pan K, Tang X, Wang W, Hu Q. 2014. *Zymomonas mobilis*: a novel platform for future biorefineries. *Biotechnol Biofuels* 7:101. <https://doi.org/10.1186/1754-6834-7-101>.
- Yang S, Fei Q, Zhang Y, Contreras LM, Utturkar SM, Brown SD, Himmel ME, Zhang M. 2016. *Zymomonas mobilis* as a model system for

- production of biofuels and biochemicals. *Microb Biotechnol* 9:699–717. <https://doi.org/10.1111/1751-7915.12408>.
4. Karsch T, Stahl U, Esser K. 1983. Ethanol production by *Zymomonas* and *Saccharomyces*, advantages and disadvantages. *Eur J Appl Microbiol Biotechnol* 18:387–391. <https://doi.org/10.1007/BF00504750>.
  5. Lee KJ, Rogers PL. 1983. The fermentation kinetics of ethanol production by *Zymomonas mobilis*. *Chem Eng J* 27:B31–B38. [https://doi.org/10.1016/0300-9467\(83\)80067-7](https://doi.org/10.1016/0300-9467(83)80067-7).
  6. Rogers PL, Lee KJ, Tribe DE. 1979. Kinetics of alcohol production by *Zymomonas mobilis* at high sugar concentrations. *Biotechnol Lett* 1: 165–170. <https://doi.org/10.1007/BF01388142>.
  7. Wang X, He Q, Yang Y, Wang J, Haning K, Hu Y, Wu B, He M, Zhang Y, Bao J, Contreras LM, Yang S. 2018. Advances and prospects in metabolic engineering of *Zymomonas mobilis*. *Metab Eng* 50:57–73. <https://doi.org/10.1016/j.ymben.2018.04.001>.
  8. Xia J, Yang Y, Liu CG, Yang S, Bai FW. 2019. Engineering *Zymomonas mobilis* for robust cellulosic ethanol production. *Trends Biotechnol* 37: 960–972. <https://doi.org/10.1016/j.tibtech.2019.02.002>.
  9. Mohagheghi A, Linger J, Smith H, Yang S, Dowe N, Pienkos PT. 2014. Improving xylose utilization by recombinant *Zymomonas mobilis* strain 8b through adaptation using 2-deoxyglucose. *Biotechnol Biofuels* 7:19. <https://doi.org/10.1186/1754-6834-7-19>.
  10. Agrawal M, Mao Z, Chen RR. 2011. Adaptation yields a highly efficient xylose-fermenting *Zymomonas mobilis* strain. *Biotechnol Bioeng* 108: 777–785. <https://doi.org/10.1002/bit.23021>.
  11. Zhang M, Eddy C, Deanda K, Finkelstein M, Picataggio S. 1995. Metabolic engineering of a pentose metabolism pathway in ethanologenic *Zymomonas mobilis*. *Science* 267:240–243. <https://doi.org/10.1126/science.267.5195.240>.
  12. Yang S, Franden MA, Brown SD, Chou YC, Pienkos PT, Zhang M. 2014. Insights into acetate toxicity in *Zymomonas mobilis* 8b using different substrates. *Biotechnol Biofuels* 7:140. <https://doi.org/10.1186/s13068-014-0140-8>.
  13. Yang Y, Hu M, Tang Y, Geng B, Qiu M, He Q, Chen S, Wang X, Yang S. 2018. Progress and perspective on lignocellulosic hydrolytic inhibitor tolerance improvement in *Zymomonas mobilis*. *Bioresour Bioprocess* 5: 6. <https://doi.org/10.1186/s40643-018-0193-9>.
  14. Zhang Y, Vera JM, Xie D, Serate J, Pohlmann E, Russell JD, Hebert AS, Coon JJ, Sato TK, Landick R. 2019. Multiomic fermentation using chemically defined synthetic hydrolyzates revealed multiple effects of lignocellulose-derived inhibitors on cell physiology and xylose utilization in *Zymomonas mobilis*. *Front Microbiol* 10:2596. <https://doi.org/10.3389/fmicb.2019.02596>.
  15. Misawa N, Yamano S, Ikenaga H. 1991. Production of  $\beta$ -carotene in *Zymomonas mobilis* and *Agrobacterium tumefaciens* by introduction of the biosynthesis genes from *Erwinia uredovora*. *Appl Environ Microbiol* 57:1847–1849. <https://doi.org/10.1128/aem.57.6.1847-1849.1991>.
  16. Yang S, Mohagheghi A, Franden MA, Chou YC, Chen X, Dowe N, Himmel ME, Zhang M. 2016. Metabolic engineering of *Zymomonas mobilis* for 2,3-butanediol production from lignocellulosic biomass sugars. *Biotechnol Biofuels* 9:189. <https://doi.org/10.1186/s13068-016-0606-y>.
  17. Kremer TA, LaSarre B, Posto AL, McKinlay JB. 2015. N<sub>2</sub> gas is an effective fertilizer for bioethanol production by *Zymomonas mobilis*. *Proc Natl Acad Sci U S A* 112:2222–2226. <https://doi.org/10.1073/pnas.1420663112>.
  18. Davis R, Grundl N, Tao L, Bidy MJ, Tan ECD, Beckham GT, Humbird D, Thompson DN, Roni MS. 2018. Process design and economics for the conversion of lignocellulosic biomass to hydrocarbon fuels and coproducts: 2018 biochemical design case update. Biochemical deconstruction and conversion of biomass to fuels and products via integrated biorefinery pathways. National Renewable Energy Laboratory, Golden, CO. <https://www.nrel.gov/docs/fy19osti/71949.pdf>.
  19. Palamae S, Choorit W, Chatsungnoen T, Chisti Y. 2020. Simultaneous nitrogen fixation and ethanol production by *Zymomonas mobilis*. *J Biotechnol* 314–315:41–52. <https://doi.org/10.1016/j.jbiotec.2020.03.016>.
  20. Alencar VC, dos de Silva JFS, Boas ROV, Farnézio VM, de Maria YNLF, Barbosa DA, Almeida AT, de Souza EM, Müller-Santos M, Jabes DL, Menegidio FB, de Oliveira RC, Rodrigues T, Tersariol IL, dos S, Walmsley AR, Nunes LR. 2021. The quorum sensing auto-inducer 2 (Al-2) stimulates nitrogen fixation and favors ethanol production over biomass accumulation in *Zymomonas mobilis*. *Int J Mol Sci* 22:5628. <https://doi.org/10.3390/ijms22115628>.
  21. Sprenger GA. 1996. Carbohydrate metabolism in *Zymomonas mobilis*: a catabolic highway with some scenic routes. *FEMS Microbiol Lett* 145: 301–307. <https://doi.org/10.1111/j.1574-6968.1996.tb08593.x>.
  22. Hebert AS, Richards AL, Bailey DJ, Ulbrich A, Coughlin EE, Westphal MS, Coon JJ. 2014. The one hour yeast proteome. *Mol Cell Proteomics* 13: 339–347. <https://doi.org/10.1074/mcp.M113.034769>.
  23. Lu W, Clasquin MF, Melamud E, Amador-Noguez D, Caudy AA, Rabinowitz JD. 2010. Metabolomic analysis via reversed-phase ion-pairing liquid chromatography coupled to a stand alone orbitrap mass spectrometer. *Anal Chem* 82:3212–3221. <https://doi.org/10.1021/ac902837x>.
  24. Yang S, Vera JM, Grass J, Savvakis G, Moskvina OV, Yang Y, McIlwain SJ, Lyu Y, Zinonos I, Hebert AS, Coon JJ, Bates DM, Sato TK, Brown SD, Himmel ME, Zhang M, Landick R, Pappas KM, Zhang Y. 2018. Complete genome sequence and the expression pattern of plasmids of the model ethanologenic *Zymomonas mobilis* ZM4 and its xylose-utilizing derivatives 8b and 2032. *Biotechnol Biofuels* 11:125. <https://doi.org/10.1186/s13068-018-1116-x>.
  25. Shishkova E, Hebert AS, Westphal MS, Coon JJ. 2018. Ultra-high pressure (>30,000 psi) packing of capillary columns enhancing depth of shotgun proteomic analyses. *Anal Chem* 90:11503–11508. <https://doi.org/10.1021/acs.analchem.8B02766>.
  26. Hebert AS, Thöing C, Riley NM, Kwicien NW, Shiskova E, Huguet R, Cardasis HL, Kuehn A, Eliuk S, Zabrouskov V, Westphal MS, McAlister GC, Coon JJ. 2018. Improved precursor characterization for data-dependent mass spectrometry. *Anal Chem* 90:2333–2340. <https://doi.org/10.1021/acs.analchem.7b04808>.
  27. Fruzangohar JM, Ebrahimie E, Ogunniyi AD, Mahdi LK, Paton JC, Adelson DL. 2013. Comparative GO: a Web application for comparative gene ontology and gene ontology-based gene selection in bacteria. *PLoS One* 8: e58759. <https://doi.org/10.1371/journal.pone.0058759>.
  28. Jacobson MR, Brigle KE, Bennett LT, Setterquist RA, Wilson MS, Cash VL, Beynon J, Newton WE, Dean DR. 1989. Physical and genetic map of the major nif gene cluster from *Azotobacter vinelandii*. *J Bacteriol* 171: 1017–1027. <https://doi.org/10.1128/jb.171.2.1017-1027.1989>.
  29. Riedel GE, Ausubel FM, Cannon FC. 1979. Physical map of chromosomal ethanologenic (nif) genes of *Klebsiella pneumoniae*. *Proc Natl Acad Sci U S A* 76:2866–2870. <https://doi.org/10.1073/pnas.76.6.2866>.
  30. Yang S, Pappas KM, Hauser LJ, Land ML, Chen GL, Hurst GB, Pan C, Kouvelis VN, Typas MA, Pelletier DA, Klingeman DM, Chang YJ, Samatova NF, Brown SD. 2009. Improved genome annotation for *Zymomonas mobilis*. *Nat Biotechnol* 27:893–894. <https://doi.org/10.1038/nbt1009-893>.
  31. Burén S, Jiménez-Vicente E, Echavarrri-Erasun C, Rubio LM. 2020. Biosynthesis of nitrogenase cofactors. *Chem Rev* 120:4921–4968. <https://doi.org/10.1021/acs.chemrev.9b00489>.
  32. Rubio LM, Ludden PW. 2008. Biosynthesis of the iron-molybdenum cofactor of nitrogenase. *Annu Rev Microbiol* 62:93–111. <https://doi.org/10.1146/annurev.micro.62.081307.162737>.
  33. Westphal L, Wiechmann A, Baker J, Minton NP, Müller V. 2018. The Rnf complex is an energy-coupled transhydrogenase essential to reversibly link cellular NADH and ferredoxin pools in the acetogen *Acetobacterium woodii*. *J Bacteriol* 200:e00357-18. <https://doi.org/10.1128/JB.00357-18>.
  34. Poudel S, Colman DR, Fixen KR, Ledbetter RN, Zheng Y, Pence N, Seefeldt LC, Peters JW, Harwood CS, Boyd ES. 2018. Electron transfer to nitrogenase in different genomic and metabolic backgrounds. *J Bacteriol* 200:e00757-17. <https://doi.org/10.1128/JB.00757-17>.
  35. Fischer H-M, Alvarez-Morales A, Henneke H. 1986. The pleiotropic nature of symbiotic regulatory mutants: *Bradyrhizobium japonicum* nifA gene is involved in control of nif gene expression and formation of determinate symbiosis. *EMBO J* 5:1165–1173. <https://doi.org/10.1002/j.1460-2075.1986.tb04342.x>.
  36. Zou X, Zhu Y, Pohlmann EL, Li J, Zhang Y, Roberts GP. 2008. Identification and functional characterization of NifA variants that are independent of GlnB activation in the photosynthetic bacterium *Rhodospirillum rubrum*. *Microbiology (Reading)* 154:2689–2699. <https://doi.org/10.1099/mic.0.2008/019406-0>.
  37. Dixon R, Kahn D. 2004. Genetic regulation of biological nitrogen fixation. *Nat Rev Microbiol* 2:621–631. <https://doi.org/10.1038/nrmicro954>.
  38. Tsoy OV, Ravcheev DA, Čuklina J, Gelfand MS. 2016. Nitrogen fixation and molecular oxygen: comparative genomic reconstruction of transcription regulation in Alphaproteobacteria. *Front Microbiol* 7:1343. <https://doi.org/10.3389/fmicb.2016.01343>.
  39. Morett E, Buck M. 1989. In vivo studies on the interaction of RNA polymerase- $\sigma$ 54 with the *Klebsiella pneumoniae* and *Rhizobium meliloti* nifH promoters. The role of NifA in the formation of an open promoter complex. *J Mol Biol* 210:65–77. [https://doi.org/10.1016/0022-2836\(89\)90291-X](https://doi.org/10.1016/0022-2836(89)90291-X).
  40. Hoover TR, Shah VK, Roberts GP, Ludden PW. 1986. nifV-dependent, low-molecular-weight factor required for in vitro synthesis of iron-

- molybdenum cofactor of nitrogenase. *J Bacteriol* 167:999–1003. <https://doi.org/10.1128/jb.167.3.999-1003.1986>.
41. Hoover TR, Imperial J, Ludden PW, Shah VK. 1988. Homocitrate cures the NifV-phenotype in *Klebsiella pneumoniae*. *J Bacteriol* 170:1978–1979. <https://doi.org/10.1128/jb.170.4.1978-1979.1988>.
  42. Seo J-S, Chong H, Park HS, Yoon K-O, Jung C, Kim JJ, Hong JH, Kim H, Kim J-H, Kil J-I, Park CJ, Oh H-M, Lee J-S, Jin S-J, Um H-W, Lee H-J, Oh S-J, Kim JY, Kang HL, Lee SY, Lee KJ, Kang HS. 2005. The genome sequence of the ethanologenic bacterium *Zymomonas mobilis* ZM4. *Nat Biotechnol* 23:63–68. <https://doi.org/10.1038/nbt1045>.
  43. Larsen SH, Adler J, Gargus JJ, Hogg RW. 1974. Chemomechanical coupling without ATP: the source of energy for motility and chemotaxis in bacteria. *Proc Natl Acad Sci U S A* 71:1239–1243. <https://doi.org/10.1073/pnas.71.4.1239>.
  44. Terashima H, Kojima S, Homma M. 2008. Flagellar motility in bacteria: structure and function of flagellar motor. *Int Rev Cell Mol Biol* 270:39–85. [https://doi.org/10.1016/S1937-6448\(08\)01402-0](https://doi.org/10.1016/S1937-6448(08)01402-0).
  45. He M, Wu B, Shui Z, Hu Q, Wang W, Tan F, Tang X, Zhu Q, Pan K, Li Q, Su X. 2012. Transcriptome profiling of *Zymomonas mobilis* under ethanol stress. *Biotechnol Biofuels* 5:75–10. <https://doi.org/10.1186/1754-6834-5-75>.
  46. Zhang K, Shao H, Cao Q, He M, Wu B, Feng H. 2015. Transcriptional analysis of adaptation to high glucose concentrations in *Zymomonas mobilis*. *Appl Microbiol Biotechnol* 99:2009–2022. <https://doi.org/10.1007/s00253-014-6342-y>.
  47. Yang Q, Yang Y, Tang Y, Wang X, Chen Y, Shen W, Zhan Y, Gao J, Wu B, He M, Chen S, Yang S. 2020. Development and characterization of acidic-pH-tolerant mutants of *Zymomonas mobilis* through adaptation and next-generation sequencing-based genome resequencing and RNA-Seq. *Biotechnol Biofuels* 13:1–17. <https://doi.org/10.1186/s13068-020-01781-1>.
  48. Martien JJ, Hebert AS, Stevenson DM, Regner MR, Khana DB, Coon JJ, Amador-Noguez D. 2019. Systems-level analysis of oxygen exposure in *Zymomonas mobilis*: implications for isoprenoid production. *mSystems* 4:e00284-18. <https://doi.org/10.1128/mSystems.00284-18>.
  49. Yang S, Franden MA, Wang X, Chou Y-C, Hu Y, Brown SD, Pienkos PT, Zhang M. 2020. Transcriptomic profiles of *Zymomonas mobilis* 8b to furfural acute and long-term stress in both glucose and xylose conditions. *Front Microbiol* 11:13. <https://doi.org/10.3389/fmicb.2020.00013>.
  50. Todhanakasem T, Yodsanga S, Sowatad A, Kanokratana P, Thanonkeo P, Champreda V. 2018. Inhibition analysis of inhibitors derived from lignocellulose pretreatment on the metabolic activity of *Zymomonas mobilis* biofilm and planktonic cells and the proteomic responses. *Biotechnol Bioeng* 115:70–81. <https://doi.org/10.1002/bit.26449>.
  51. Moat AG, Foster JW, Spector MP. 2002. *Microbial physiology*, 4th ed. Wiley-Liss, Hoboken, NJ.
  52. Kleinschmidt JA, Kleiner D. 1978. The glutamine synthetase from *Azotobacter vinelandii*: purification, characterization, regulation and localization. *Eur J Biochem* 89:51–60. <https://doi.org/10.1111/j.1432-1033.1978.tb20895.x>.
  53. Vanoni MA, Curti B. 1999. Glutamate synthase: a complex iron-sulfur flavoprotein. *Cell Mol Life Sci* 55:617–638. <https://doi.org/10.1007/s000180050319>.
  54. Veronese FM, Boccu E, Conventi L. 1975. Glutamate dehydrogenase from *Escherichia coli*: induction, purification and properties of the enzyme. *Biochim Biophys Acta* 377:217–228. [https://doi.org/10.1016/0005-2744\(75\)90304-6](https://doi.org/10.1016/0005-2744(75)90304-6).
  55. Meek TD, Villafranca JJ. 1980. Kinetic mechanism of *Escherichia coli* glutamine synthetase. *Biochemistry* 19:5513–5519. <https://doi.org/10.1021/bi00565a008>.
  56. van Heeswijk WC, Westerhoff HV, Booger FC. 2013. Nitrogen assimilation in *Escherichia coli*: putting molecular data into a systems perspective. *Microbiol Mol Biol Rev* 77:628–695. <https://doi.org/10.1128/MMBR.00025-13>.
  57. Helling RB. 1998. Pathway choice in glutamate synthesis in *Escherichia coli*. *J Bacteriol* 180:4571–4575. <https://doi.org/10.1128/JB.180.17.4571-4575.1998>.
  58. Lee KY, Park JM, Kim TY, Yun H, Lee SY. 2010. The genome-scale metabolic network analysis of *Zymomonas mobilis* ZM4 explains physiological features and suggests ethanol and succinic acid production strategies. *Microb Cell Fact* 9:94. <https://doi.org/10.1186/1475-2859-9-94>.
  59. Woods DR, Reid SJ. 1993. Recent developments on the regulation and structure of glutamine synthetase enzymes from selected bacterial groups. *FEMS Microbiol Rev* 11:273–283. <https://doi.org/10.1111/j.1574-6976.1993.tb00001.x>.
  60. Tatli M, Hebert AS, Coon JJ, Amador-Noguez D. 2019. Genome wide phosphoproteome analysis of *Zymomonas mobilis* under anaerobic, aerobic, and N<sub>2</sub>-fixing conditions. *Front Microbiol* 10:1986. <https://doi.org/10.3389/fmicb.2019.01986>.
  61. Yuan J, Doucette CD, Fowler WU, Feng X-J, Piazza M, Rabitz HA, Wingreen NS, Rabinowitz JD. 2009. Metabolomics-driven quantitative analysis of ammonia assimilation in *E. coli*. *Mol Syst Biol* 5:302. <https://doi.org/10.1038/msb.2009.60>.
  62. Kanemoto RH, Ludden PW. 1987. Amino acid concentrations in *Rhodospirillum rubrum* during expression and switch-off of nitrogenase activity. *J Bacteriol* 169:3035–3043. <https://doi.org/10.1128/jb.169.7.3035-3043.1987>.
  63. Jonsson A, Nordlund S, Teixeira PF. 2009. Reduced activity of glutamine synthetase in *Rhodospirillum rubrum* mutants lacking the adenylyltransferase GlnE. *Res Microbiol* 160:581–584. <https://doi.org/10.1016/j.resmic.2009.09.003>.
  64. Kingdon HS, Shapiro BM, Stadtman ER. 1967. Regulation of glutamine synthetase. 8. ATP: glutamine synthetase adenylyltransferase, an enzyme that catalyzes alterations in the regulatory properties of glutamine synthetase. *Proc Natl Acad Sci U S A* 58:1703–1710. <https://doi.org/10.1073/pnas.58.4.1703>.
  65. Merrick MJ, Edwards RA. 1995. Nitrogen control in bacteria. *Microbiol Rev* 59:604–622. <https://doi.org/10.1128/mr.59.4.604-622.1995>.
  66. Forchhammer K. 2007. Glutamine signalling in bacteria. *Front Biosci* 12:358–370. <https://doi.org/10.2741/2069>.
  67. Kim M, Zhang Z, Okano H, Yan D, Groisman A, Hwa T. 2012. Need-based activation of ammonium uptake in *Escherichia coli*. *Mol Syst Biol* 8:616. <https://doi.org/10.1038/msb.2012.46>.
  68. Pope MR, Murrell SA, Ludden PW. 1985. Covalent modification of the iron protein of nitrogenase from *Rhodospirillum rubrum* by adenosine diphosphoribosylation of a specific arginine residue. *Proc Natl Acad Sci U S A* 82:3173–3177. <https://doi.org/10.1073/pnas.82.10.3173>.
  69. Fitzmaurice WP, Saari LL, Lowery RG, Ludden PW, Roberts GP. 1989. Genes coding for the reversible ADP-ribosylation system of dinitrogenase reductase from *Rhodospirillum rubrum*. *Mol Gen Genet* 218:340–347. <https://doi.org/10.1007/BF00331287>.
  70. Huergo LF, Pedrosa FO, Muller-Santos M, Chubatsu LS, Monteiro RA, Merrick M, Souza EM. 2012. PII signal transduction proteins: pivotal players in post-translational control of nitrogenase activity. *Microbiology (Reading)* 158:176–190. <https://doi.org/10.1099/mic.0.049783-0>.
  71. Sandmeier E, Hale TI, Christen P. 1994. Multiple evolutionary origin of pyridoxal-5'-phosphate-dependent amino acid decarboxylases. *Eur J Biochem* 221:997–1002. <https://doi.org/10.1111/j.1432-1033.1994.tb18816.x>.
  72. Brochier CÉ, López-García P, Moreira D. 2004. Horizontal gene transfer and archaeal origin of deoxyhypusine synthase homologous genes in bacteria. *Gene* 330:169–176. <https://doi.org/10.1016/j.gene.2004.01.018>.
  73. Hamana K, Matsuzaki S. 1993. Polyamine distribution patterns serve as a phenotypic marker in the chemotaxonomy of the Proteobacteria. *Can J Microbiol* 39:304–310. <https://doi.org/10.1139/m93-043>.
  74. Becerra-Rivera VA, Dunn MF. 2019. Polyamine biosynthesis and biological roles in rhizobia. *FEMS Microbiol Lett* 366:fnz084. <https://doi.org/10.1093/femsle/fnz084>.
  75. Mattoo AK, Fatima T, Upadhyay RK, Handa AK. 2015. Polyamines in plants: biosynthesis from arginine, and metabolic, physiological and stress-response roles, p 177–194. *In* D'Mello JPF (ed), *Amino acids in higher plants*. CABI, Oxfordshire, England.
  76. Shaw FL, Elliott KA, Kinch LN, Fuell C, Phillips MA, Michael AJ. 2010. Evolution and multifarious horizontal transfer of an alternative biosynthetic pathway for the alternative polyamine sym-homospermidine. *J Biol Chem* 285:14711–14723. <https://doi.org/10.1074/jbc.M110.107219>.
  77. Michael AJ. 2016. Biosynthesis of polyamines and polyamine-containing molecules. *Biochem J* 473:2315–2329. <https://doi.org/10.1042/BCJ20160185>.
  78. Burnat M, Li B, Kim SH, Michael AJ, Flores E. 2018. Homospermidine biosynthesis in the cyanobacterium *Anabaena* requires a deoxyhypusine synthase homologue and is essential for normal diazotrophic growth. *Mol Microbiol* 109:763–780. <https://doi.org/10.1111/mmi.14006>.
  79. Cunin R, Glansdorff N, Piérard A, Stalon V. 1986. Biosynthesis and metabolism of arginine in bacteria. *Microbiol Rev* 50:314–352. <https://doi.org/10.1128/mr.50.3.314-352.1986>.
  80. Oshima T. 2015. Roles of polyamines in thermophiles, p 179–188. *In* Li F-L (ed), *Thermophilic microorganisms*. Caister Academic Press, Poole, United Kingdom.
  81. Chattopadhyay MK, Tabor CW, Tabor H. 2003. Polyamines protect *Escherichia coli* cells from the toxic effect of oxygen. *Proc Natl Acad Sci U S A* 100:2261–2265. <https://doi.org/10.1073/pnas.2627990100>.



82. Chattopadhyay MK, Tabor H. 2013. Polyamines are critical for the induction of the glutamate decarboxylase-dependent acid resistance system in *Escherichia coli*. *J Biol Chem* 288:33559–33570. <https://doi.org/10.1074/jbc.M113.510552>.
83. Zhao L, Chang W, Xiao Y, Liu H, Liu P. 2013. Methylerythritol phosphate pathway of isoprenoid biosynthesis. *Annu Rev Biochem* 82:497–530. <https://doi.org/10.1146/annurev-biochem-052010-100934>.
84. Flores-Pérez U, Sauret-Güeto S, Gas E, Jarvis P, Rodríguez-Concepción M. 2008. A mutant impaired in the production of plastome-encoded proteins uncovers a mechanism for the homeostasis of isoprenoid biosynthetic enzymes in *Arabidopsis* plastids. *Plant Cell* 20:1303–1315. <https://doi.org/10.1105/tpc.108.058768>.
85. Jacobson TB, Adamczyk PA, Stevenson DM, Regner M, Ralph J, Reed JL, Amador-Noguez D. 2019. <sup>2</sup>H and <sup>13</sup>C metabolic flux analysis elucidates in vivo thermodynamics of the ED pathway in *Zymomonas mobilis*. *Metab Eng* 54:301–316. <https://doi.org/10.1016/j.ymben.2019.05.006>.
86. Flamholz A, Noor E, Bar-Even A, Liebermeister W, Milo R. 2013. Glycolytic strategy as a tradeoff between energy yield and protein cost. *Proc Natl Acad Sci U S A* 110:10039–10044. <https://doi.org/10.1073/pnas.1215283110>.
87. Wills C, Kratofil P, Londo D, Martin T. 1981. Characterization of the two alcohol dehydrogenases of *Zymomonas mobilis*. *Arch Biochem Biophys* 210:775–785. [https://doi.org/10.1016/0003-9861\(81\)90245-9](https://doi.org/10.1016/0003-9861(81)90245-9).
88. Kinoshita S, Kakizono T, Kadota K, Das K, Taguchi H. 1985. Purification of two alcohol dehydrogenases from *Zymomonas mobilis* and their properties. *Appl Microbiol Biotechnol* 22:249–254. <https://doi.org/10.1007/BF00252025>.
89. Neale AD, Scopes RK, Kelly JM, Wettenhall REH, Scopes RK. 1986. The two alcohol dehydrogenases of *Zymomonas mobilis* purification by differential dye ligand chromatography, molecular characterisation and physiological roles. *Eur J Biochem* 154:119–124. <https://doi.org/10.1111/j.1432-1033.1986.tb09366.x>.
90. Kalnenieks U, Galinina N, Toma MM, Pickford JL, Rutkis R, Poole RK. 2006. Respiratory behaviour of a *Zymomonas mobilis* adhB::kan' mutant supports the hypothesis of two alcohol dehydrogenase isoenzymes catalysing opposite reactions. *FEBS Lett* 580:5084–5088. <https://doi.org/10.1016/j.febslet.2006.08.034>.
91. Kalnenieks U, Balodite E, Strähler S, Strazdina I, Rex J, Pentjuss A, Fuchino K, Bruheim P, Rutkis R, Pappas KM, Poole RK, Sawodny O, Bettenbrock K. 2019. Improvement of acetaldehyde production in *Zymomonas mobilis* by engineering of its aerobic metabolism. *Front Microbiol* 10:2533. <https://doi.org/10.3389/fmicb.2019.02533>.
92. Xu J, Martien J, Gilbertson C, Ma J, Amador-Noguez D, Park JO. 2020. Metabolic flux analysis and fluxomics-driven determination of reaction free energy using multiple isotopes. *Curr Opin Biotechnol* 64:151–160. <https://doi.org/10.1016/j.copbio.2020.02.018>.
93. Noor E, Bar-Even A, Flamholz A, Reznik E, Liebermeister W, Milo R. 2014. Pathway thermodynamics highlights kinetic obstacles in central metabolism. *PLoS Comput Biol* 10:e1003483. <https://doi.org/10.1371/journal.pcbi.1003483>.
94. Jacobson TB, Korosh TK, Stevenson DM, Foster C, Maranas C, Olson DG, Lynd LR, Amador-Noguez D. 2020. In vivo thermodynamic analysis of glycolysis in *Clostridium thermocellum* and *Thermoanaerobacterium saccharolyticum* using <sup>13</sup>C and <sup>2</sup>H tracers. *mSystems* 5:e00736-19. <https://doi.org/10.1128/mSystems.00736-19>.
95. Park JO, Tanner LB, Wei MH, Khana DB, Jacobson TB, Zhang Z, Rubin SA, Li SHJ, Higgins MB, Stevenson DM, Amador-Noguez D, Rabinowitz JD. 2019. Near-equilibrium glycolysis supports metabolic homeostasis and energy yield. *Nat Chem Biol* 15:1001–1008. <https://doi.org/10.1038/s41589-019-0364-9>.
96. Martínez-Noël G, Curatti L, Hernandez JA, Rubio LM. 2011. NifB and NifEN protein levels are regulated by CIPX2 under nitrogen fixation conditions in *Azotobacter vinelandii*. *Mol Microbiol* 79:1182–1193. <https://doi.org/10.1111/j.1365-2958.2011.07540.x>.
97. Palma M, Madeira SC, Mendes-Ferreira A, Sá-Correia I. 2012. Impact of assimilable nitrogen availability in glucose uptake kinetics in *Saccharomyces cerevisiae* during alcoholic fermentation. *Microb Cell Fact* 11:99. <https://doi.org/10.1186/1475-2859-11-99>.
98. Chubukov V, Sauer U. 2014. Environmental dependence of stationary-phase metabolism in *Bacillus subtilis* and *Escherichia coli*. *Appl Environ Microbiol* 80:2901–2909. <https://doi.org/10.1128/AEM.00061-14>.
99. Doucette CD, Schwab DJ, Wingreen NS, Rabinowitz JD. 2011.  $\alpha$ -Ketoglutarate coordinates carbon and nitrogen utilization via enzyme inhibition. *Nat Chem Biol* 7:894–901. <https://doi.org/10.1038/nchembio.685>.
100. Jones CW, Doelle HW. 1991. Kinetic control of ethanol production by *Zymomonas mobilis*. *Appl Microbiol Biotechnol* 35:4–9. <https://doi.org/10.1007/BF00180626>.
101. Weir PM. 2016. The ecology of *Zymomonas*: a review. *Folia Microbiol (Praha)* 61:385–392. <https://doi.org/10.1007/s12223-016-0447-x>.
102. Barnell WO, Yi KC, Conway T. 1990. Sequence and genetic organization of a *Zymomonas mobilis* gene cluster that encodes several enzymes of glucose metabolism. *J Bacteriol* 172:7227–7240. <https://doi.org/10.1128/jb.172.12.7227-7240.1990>.
103. Li M, Hou F, Wu T, Jiang X, Li F, Liu H, Xian M, Zhang H. 2020. Recent advances of metabolic engineering strategies in natural isoprenoid production using cell factories. *Nat Prod Rep* 37:80–99. <https://doi.org/10.1039/c9np00016j>.
104. Du D, Tan L, Wang Y, Peng B, Weinstein JN, Wondisford FE, Su X, Lorenzi PL. 2019. ElemCor: accurate data analysis and enrichment calculation for high-resolution LC-MS stable isotope labeling experiments. *BMC Bioinformatics* 20:1–9. <https://doi.org/10.1186/s12859-019-2669-9>.
105. Young JD. 2014. INCA: a computational platform for isotopically non-stationary metabolic flux analysis. *Bioinformatics* 30:1333–1335. <https://doi.org/10.1093/bioinformatics/btu015>.
106. Antoniewicz MR, Kelleher JK, Stephanopoulos G. 2007. Elementary metabolite units (EMU): a novel framework for modeling isotopic distributions. *Metab Eng* 9:68–86. <https://doi.org/10.1016/j.ymben.2006.09.001>.
107. Leighty RW, Antoniewicz MR. 2013. COMPLETE-MFA: complementary parallel labeling experiments technique for metabolic flux analysis. *Metab Eng* 20:49–55. <https://doi.org/10.1016/j.ymben.2013.08.006>.
108. Pisithkul T, Schroeder JW, Trujillo EA, Yeasin P, Stevenson DM, Chaiamarit T, Coon JJ, Wang JD, Amador-Noguez D. 2019. Metabolic remodeling during biofilm development of *Bacillus subtilis*. *mBio* 10:e00623-19. <https://doi.org/10.1128/mBio.00623-19>.
109. Clasquin MF, Melamud E, Rabinowitz JD, Clasquin MF, Melamud E, Rabinowitz JD. 2012. LC-MS data processing with MAVEN: a metabolomic analysis and visualization engine. *Curr Protoc Bioinformatics Chapter 14:Unit14.11*. <https://doi.org/10.1002/0471250953.bi1411s37>.
110. Cox J, Mann M. 2008. MaxQuant enables high peptide identification rates, individualized p.p.b.-range mass accuracies and proteome-wide protein quantification. *Nat Biotechnol* 26:1367–1372. <https://doi.org/10.1038/nbt.1511>.
111. Benjamini Y, Hochberg Y. 1995. Controlling the false discovery rate: a practical and powerful approach to MultipleSource. *J R Stat Soc Ser B (Methodological)* 57:289–300. <https://doi.org/10.1111/j.2517-6161.1995.tb02031.x>.
112. Vizcaíno JA, Csordas A, del-Toro N, Dienes JA, Griss J, Lavidas I, Mayer G, Perez-Riverol Y, Reisinger F, Ternent T, Xu Q-W, Wang R, Hermjakob H. 2016. 2016 update of the PRIDE database and its related tools. *Nucleic Acids Res* 44:11033–11033. <https://doi.org/10.1093/nar/gkw880>.
113. Foster ED, Deardorff A. 2017. Open Science Framework (OSF). *J Med Libr Assoc* 105:203.
114. Qiu M, Shen W, Yan X, He Q, Cai D, Chen S, Wei H, Knoshaug EP, Zhang M, Himmel ME, Yang S. 2020. Metabolic engineering of *Zymomonas mobilis* for anaerobic isobutanol production. *Biotechnol Biofuels* 13:15. <https://doi.org/10.1186/s13068-020-1654-x>.
115. Liu Y, Ghosh IN, Martien J, Zhang Y, Amador-Noguez D, Landick R. 2020. Regulated redirection of central carbon flux enhances anaerobic production of bio-products in *Zymomonas mobilis*: rewiring central carbon flux in *Z. mobilis*. *Metab Eng* 61:261–274. <https://doi.org/10.1016/j.ymben.2020.06.005>.